

## Anonymous Referee #1

We thank the reviewer again for the comments to improve our understanding and the manuscript. For Methodology, we add more explanation to justify its validity. For results to conclusion, we make it clearer in the response. Please see our detailed response below.

### *Specific comments:*

- *1) 'Smooth' topography?*

*The authors argued that their method (applying single value to 5 by r grids) produces a smoothed topography by presenting an example. But I have to say that the example is misleading.*

*Considering a simple case, 10 grids at 4 km spacing have elevation values of (0, 1, 2, 3, 4), (5, 6, 7, 8, 9) along a horizontal dimension, meaning a constant slope of 1/4. After applying their method, so these grids turn to have values (2, 2, 2, 2, 2), (7, 7, 7, 7, 7). Now, the slopes are 0, 0, 0, 0, 5/4, 0, 0, 0, 0. As such, will you state that the topography is smoothed through their method? On the contrary, in this case a smooth topography becomes unsmooth (as being stepped) after applying their 'smoothing' method.*

*So, their methodology fails at all.*

Thanks for the reviewer to raise this point. We re-checked our smoothing methodology and found that our previous statement is incorrect. We actually bilinearly interpolated the topography data of the grid cells at 20-km resolution into the grid cells at 4-km. We select a 10x10 grid cells at 4 km resolution and the corresponding 2x2 grid cells at 20 km resolution over the Himalayas region as an example (Fig. R1). It is evident the “smooth” topography is smoother. Sorry for the misleading and the text is revised as “Therefore, besides this control experiment, one sensitivity (idealized) experiment is also conducted with the same configuration as the control one except that the terrain heights of the inner domain at 4-km resolution are bilinearly interpolated from the terrain heights at 20-km resolution similar as previous studies (e.g., Shi et al., 2008; Wu et al., 2012b; Lin et al., 2018).”

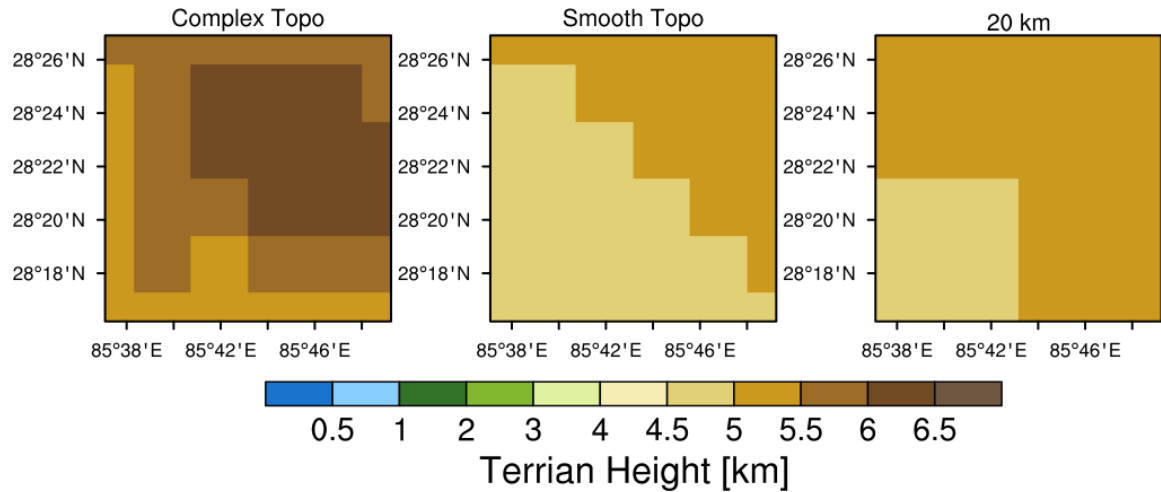


**Figure R1.** Spatial distributions of terrain height from the dataset at 4-km resolution (Complex Topo), bilinearly interpolated from the 20-km resolution dataset (Smooth Topo), and from the original 20-km resolution dataset.

In order to further prove that our methodology serves the purpose to smooth the complex topography of Himalayas region with many mountains and valleys, we analyze the slopes between the neighboring grids in our simulation domain (the new figure is added as Fig. S2 in the supporting material). It is pretty evident that after applying our methodology, the slopes between the neighboring grids are much lower with the smooth topography than with the complex topography in general, particularly over the Himalayas region. We do find the slopes of a few grids increase after “smoothing”, but the portion is very small. We believe this is convincing that after applying our method, the topography becomes much smoother overall. Now, we add the clarification in the revised manuscript as

“In addition, the slopes between the neighboring grids are significantly reduced in general with the smooth topography compared to with the complex topography, particularly over the Himalayas region (Fig. S2 in the supporting material).”

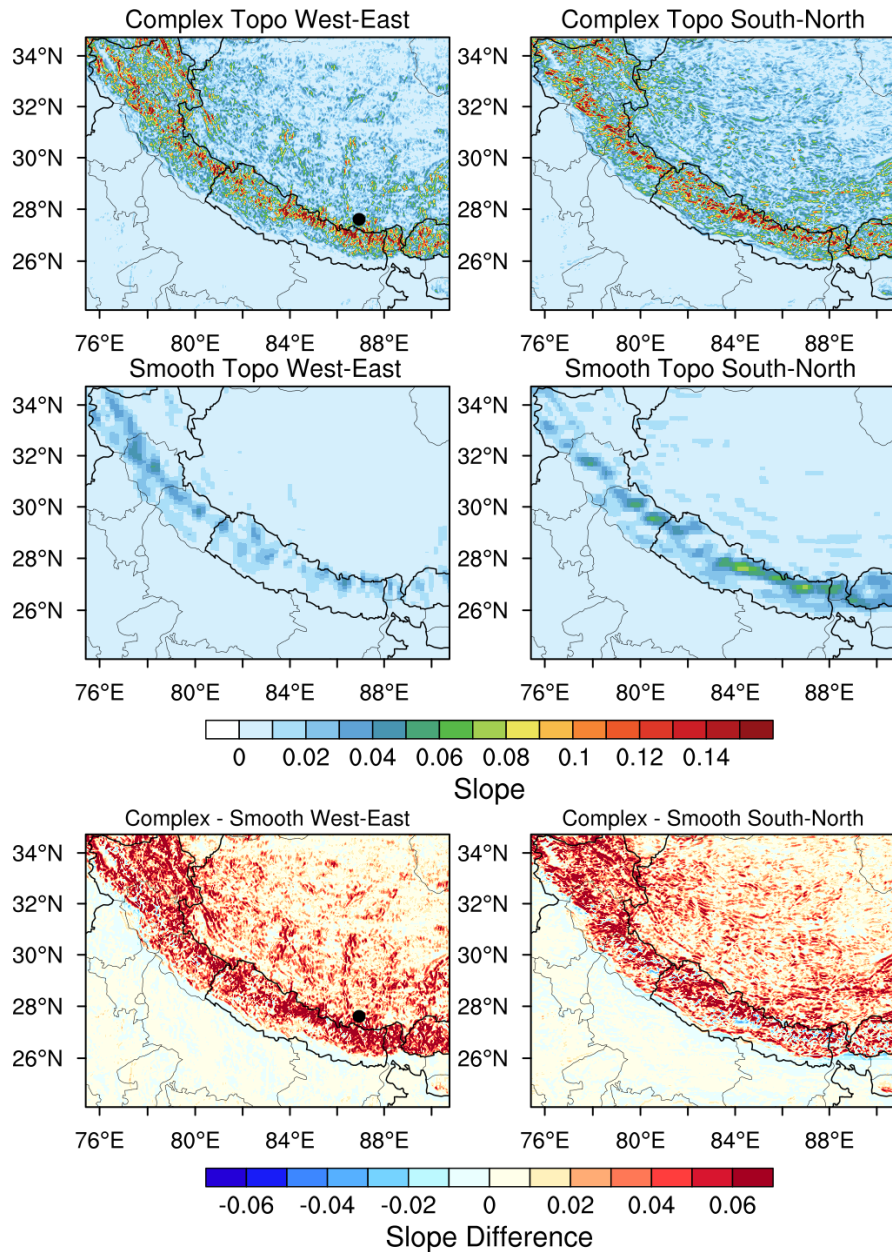


**Figure S2.** The slopes between the neighboring grids in our 4-km simulation domain with the complex and smooth topography. The slopes are calculated in west-east and south-north direction by the formula:  $\text{slope} = |(z_1 - z_2) / dx|$ , where  $z_1$  and  $z_2$  denote the terrain heights (in km) of the two neighboring grids and  $dx$  is 4 km.

- 2) “which come first, chicken or egg?”.  
*The authors intended to conclude that the wind difference between simulations of different representation of topography leads to BC transport difference and further BC concentration difference. The reviewer found from their results that*

*BC transport difference is rather contributed by the BC concentration difference simulated. Then the authors argued that this is a “which come first, chicken or egg?” question.*

*Well, the problem is not that the reviewer raised such a question but that the question comes from the non-linear nature. If the authors want to draw the such conclusion, they have to find a way circumventing it, as the magnitude of BC transport is determined by both wind and concentration (or mass). That is, the authors have to strictly prove that BC transport is the only factor affecting the BC concentration tendency so that to make their conclusion ('the wind difference between simulations of different representation of topography leads to BC transport difference and further BC concentration difference') valid.*

We have proved our statement that the wind difference is the key factor influencing the transport in our last response to the reviewer’s comment. Here, we clarify it again as following.

We provide the evidence about the enhancement of southerly wind due to the complex topography in the last version of revised manuscript, in which one new figure (Fig. 13) is added into the main text about the changes of near-surface meridional wind during our simulation period due to the impacts of complex topography. The near-surface southerly wind during the daytime of simulation period is increased with the complex topography over the Himalayas (Fig. 13), which indicates that the transport towards the TP is strengthened with the complex topography in the study period, particularly over the central and eastern Himalayas which is near the source region of high BC mass loading.

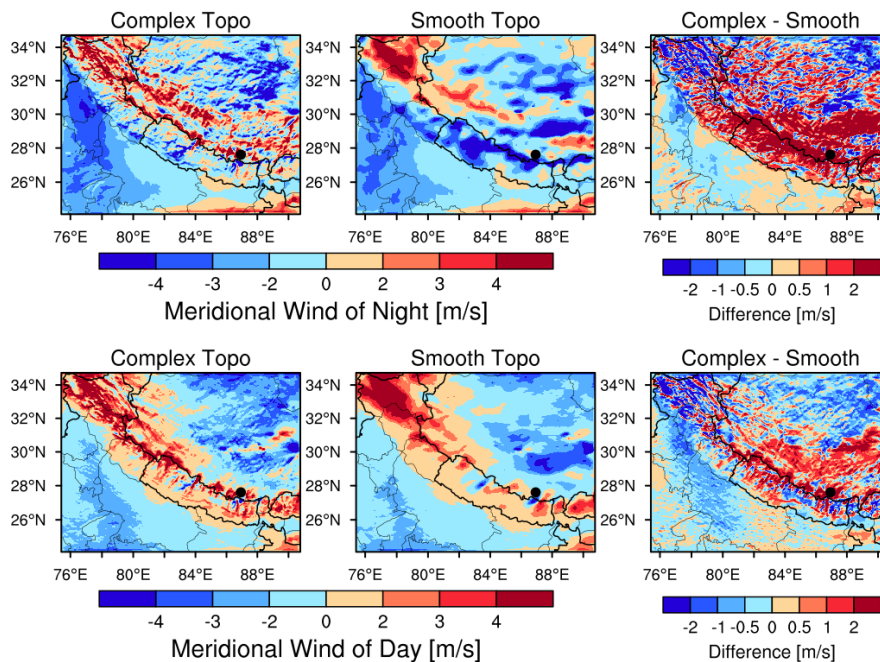


**Figure 13.** Spatial distributions of meridional wind speed averaged within 500 m above the ground for day and night during April 1-20, 2016 from the simulations with complex and smooth topography. The difference between the two is also shown. Nighttime is

defined as local time 21:00-6:00, and daytime is defined as 9:00-18:00. Positive value denotes southerly, and negative value denotes northerly.

The Himalayas and TP regions are relatively clean. The BC mass is mostly transported from the source region of South Asia, which can be reflected from both emissions (Fig. 1) and satellite retrievals (Fig. 6). As the reviewer stated, the higher mass over the source region may also lead to stronger transported mass even if the wind does not change. We have shown that the BC column mass loading is actually lower over the source region from the simulation with the complex topography compared to that with the smooth topography (Fig. 5). This can prove that the stronger mass transport is not due to the higher mass loading over the source region in the simulation with the complex topography. In fact, this can reflect that the stronger transport with the complex topography reduces the mass loading over the source region and increases the mass loading over the relatively clean region over the Himalayas and TP.

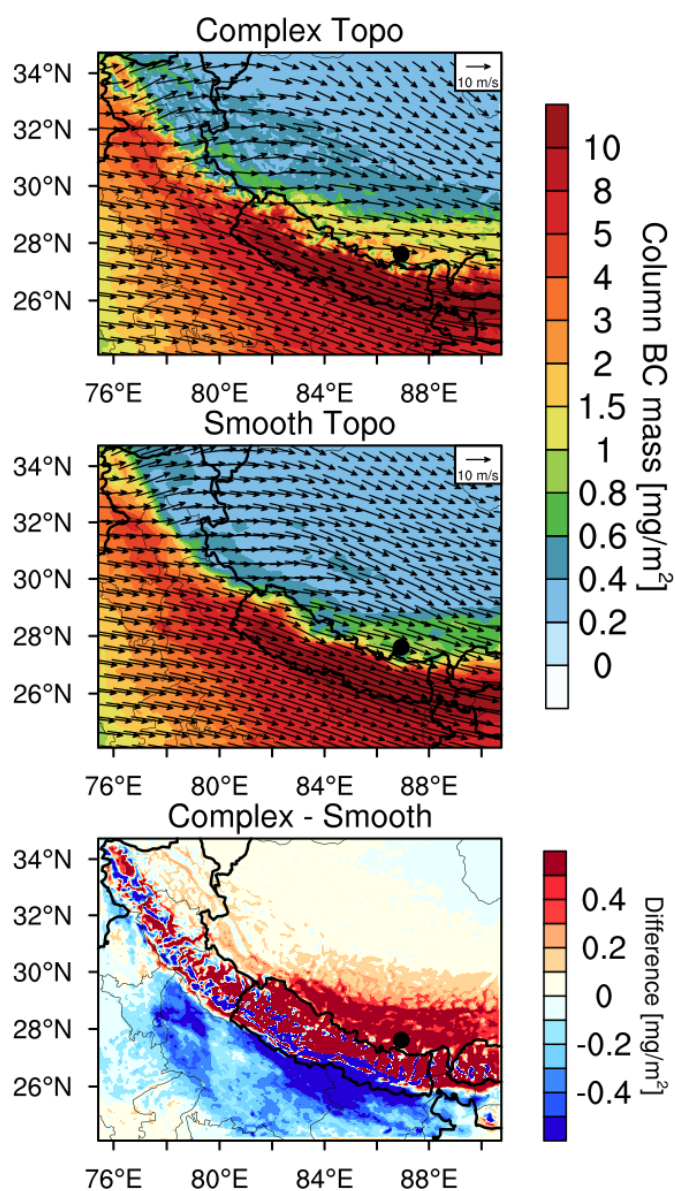


**Figure 5.** Spatial distributions of column integrated BC mass and the horizontal wind field at 500 hPa from the simulations with complex and smooth topography (Complex Topo and Smooth Topo) averaged for April 1-20, 2016. The difference between the two is also shown.

Based on the evidence and discussion above, we conclude that one key factor leading to the stronger transport with the complex topography is the strengthened efficiency of near-surface meridional transport towards the TP in the study period.



# 1 **Impact of topography on black carbon transport to the southern Tibetan** 2 **Plateau during pre-monsoon season and its climatic implication**

3 <sup>1</sup>Meixin Zhang, <sup>1</sup>Chun Zhao\*, <sup>2,3</sup>Zhiyuan Cong, <sup>1</sup>Qiuyan Du, <sup>1</sup>Mingyue Xu, <sup>1</sup>Yu Chen, <sup>4</sup>Ming  
4 Chen, <sup>1</sup>Rui Li, <sup>1</sup>Yunfei Fu, <sup>1</sup>Lei Zhong, <sup>3,5</sup>Shichang Kang, <sup>6</sup>Delong Zhao, <sup>6</sup>Yan Yang

5  
6  
7 <sup>1</sup>School of Earth and Space Sciences, University of Science and Technology of China, Hefei,  
8 China

9 <sup>2</sup>Key Laboratory of Tibetan Environment Changes and Land Surface Processes, Institute of  
10 Tibetan Plateau Research, Chinese Academy of Sciences (CAS), Beijing 100101, China

11 <sup>3</sup>CAS Center for Excellence in Tibetan Plateau Earth Sciences, Institute of Tibetan Plateau  
12 Research, CAS, Beijing 100101, China

13 <sup>4</sup>National Center for Atmospheric Research, Boulder, CO, USA

14 <sup>5</sup>State Key Laboratory of Cryosphere Science, Northwest Institute of Eco-Environment and  
15 Resources, CAS, Lanzhou 730000, China

16 <sup>6</sup>Beijing Weather Modification Office, Beijing 100101, China

17  
18 Manuscript for submission to Atmos. Chem. Phys.

19  
20  
21 \*Corresponding author: Chun Zhao (chunzhao@ustc.edu.cn)

## 22 23 **Key points:**

24 1. The black carbon (BC) transport across the Himalayas can overcome a majority of  
25 mountain ridges, but the valley transport is much more efficient during the pre-monsoon  
26 season.  
27

28 2. The complex topography results in stronger overall crossing-Himalayas transport during  
29 the study period primarily due to the strengthened efficiency of near-surface meridional  
30 transport towards the TP, enhanced wind speed at some valleys, and deeper valley channels  
31 associated with larger transported BC mass volume.

32 3. The complex topography generates 50% higher transport flux of BC across the Himalayas  
33 and 30-50% stronger BC radiative heating in the atmosphere up to 10 km over the Tibetan  
34 Plateau (TP) than that with the smoother topography, which implies that global climate  
35 models with relatively coarse resolution may introduce significant negative biases in  
36 estimating BC radiative forcing over the TP due to smooth topography.

37 4. The different topography also leads to different distributions of snow cover and BC forcing  
38 in snow over the TP.

40 **Abstract**

41 Most of previous modeling studies about black carbon (BC) transport and impact over  
42 the Tibetan Plateau (TP) conducted simulations with horizontal resolutions coarser than 10  
43 km that may not be able to resolve well the complex topography of the Himalayas. In this  
44 study, the two experiments covering entire Himalayas with the Weather Research and  
45 Forecasting Model coupled with chemistry (WRF-Chem) at the horizontal resolution of 4 km  
46 but with two different topography datasets (4-km complex topography and 20-km smooth  
47 topography) are conducted for pre-monsoon season (April, 2016) to investigate the impacts  
48 of topography on modeling the transport and distribution of BC over the TP. Both  
49 experiments show evident accumulation of aerosols near the southern Himalayas during the  
50 pre-monsoon season, consistent with the satellite retrievals. The observed episode of high  
51 near-surface BC concentration at the station near the Mt. Everest due to heavy biomass  
52 burning near the southern Himalayas is well captured by the simulations. The simulations  
53 indicate that the prevailing up-flow across the Himalayas driven by the large-scale westerly  
54 and small-scale southerly circulations during the daytime is the dominant transport  
55 mechanism of South Asian BC into the TP, and is much stronger than that during the  
56 nighttime. The simulation with 4-km topography resolves more valleys and mountain ridges,  
57 and shows that the BC transport across the Himalayas can overcome a majority of mountain  
58 ridges but the valley transport is more efficient. The complex topography results in stronger  
59 overall crossing-Himalayas transport during the simulation period primarily due to the  
60 strengthened efficiency of near-surface meridional transport towards the TP, enhanced wind  
61 speed at some valleys, and deeper valley channels associated with larger transported BC mass  
62 volume. This results in 50% higher transport flux of BC across the Himalayas and 30-50%  
63 stronger BC radiative heating in the atmosphere up to 10 km over the TP from the simulation  
64 with 4-km complex topography than that with 20-km smoother topography. The different  
65 topography also leads to different distributions of snow cover and BC forcing in snow. This  
66 study implies that global climate models generally with even coarser resolutions than 20 km  
67 and therefore relatively smoother topography may introduce significant negative biases in  
68 estimating light absorbing aerosol radiative forcing over the TP.

69  
70  
71  
72  
73



## 74 **1. Introduction**

75 The Tibetan Plateau (TP) is the highest plateau in the world with an average elevation  
76 over 4 km and an area of approximately  $2.5 \times 10^6 \text{ km}^2$ , known as the world's third pole (Qiu,  
77 2008), and its enormous dynamic and thermal effects have a huge impact on large-scale  
78 atmospheric circulation through the energy exchange with the atmosphere especially the  
79 troposphere, such as Asian monsoon (e.g., Ye and Wu, 1998; Duan and Wu, 2005; Wu et al.,  
80 2007, 2012a; Boos and Kuang, 2013; Chen and Bordoni, 2014; He et al., 2019; Zhao et al.,  
81 2019). In addition, the glacial melting water of TP is one of the important sources of water  
82 resources of the Indus River, Ganges River, Yangtze River, and Yellow River in Asia (e.g.,  
83 Singh and Bengtsson, 2004; Barnett et al., 2005; Immerzeel et al., 2010; Lutz et al., 2014).  
84 Previous studies found aerosols in the atmosphere over/around the TP could change the  
85 regional climate of Asia (e.g., Qian et al., 2011, 2015; Lau et al., 2017, 2018). Model  
86 simulations showed that the absorptive aerosols changed the surface radiative flux over the  
87 TP by  $5\text{-}25 \text{ W m}^{-2}$  during the pre-monsoon season in April and May and led to the changes in  
88 summer monsoon circulations (Qian et al., 2011). Meanwhile, aerosol may affect the  
89 atmosphere by modulating the vertical structure of cloud and precipitation around the TP, and  
90 thus change the distribution of atmospheric latent heat around the TP, which is the main  
91 driving force of regional atmosphere circulations (e.g., Li et al., 2010, 2017, 2019). Moreover,  
92 when absorbing aerosols settle on the snow-covered areas, they will blacken the surface of  
93 snow cover and glacier to a large extent (e.g., Hansen and Nazarenko, 2004; Ramanathan and  
94 Carmichael, 2008; Lau et al., 2010, 2018; Lee et al., 2013; Zhang et al., 2017, 2018), reduce  
95 the snow albedo so as to absorb more solar radiation and cause the consequences of  
96 accelerated melting (e.g., Ramanathan et al., 2007; Ming et al., 2009; Yasunari et al., 2010; Ji  
97 et al., 2015; Zhang et al., 2015). According to the Intergovernmental Panel on Climate  
98 Change Fifth Assessment Report (IPCC AR5), the radiative forcing caused by the important  
99 component of absorbing aerosols, black carbon (BC), on the surface snow is  $0.04 \text{ W m}^{-2}$   
100 ( $0.02\text{-}0.09 \text{ W m}^{-2}$ ) on global average, and the regional forcing (such as over the Arctic and  
101 the Himalayas) can be considerably large.

102 The TP is surrounded by various sources of pollutants. Over the South of TP, previous  
103 studies have suggested that South Asia was the main source of pollutants transported to the  
104 plateau (e.g., Cong et al., 2009, 2015a, b; Kopacz et al., 2011; Lu et al., 2012; Zhao et al.,  
105 2013; Wang et al., 2015; Zhang et al., 2015; Kang et al., 2016, 2019; Li et al., 2016; Chen et  
106 al., 2018). A huge blanket or layer of “haze” composes of light-absorbing carbonaceous

107 aerosol particles that often erupts in the pre-monsoon season over South Asia and has a  
108 significant influence on the plateau (e.g., Prasad and Singh, 2007; Engling and Gelencser,  
109 2010). Among them, biomass burning emission reaching the maximum in pre-monsoon  
110 season over South Asia is one of the dominant sources (e.g., Cong et al., 2015b). Many  
111 studies investigated the transport mechanisms of South Asian pollutants to the TP and found  
112 that the pollutants transported across the Himalayas were mainly due to the combination of  
113 large-scale circulation and regional wind (e.g., Hindman and Upadhyay, 2002; Cao et al.,  
114 2010; Dumka et al., 2010; Marinoni et al., 2010; Cong et al., 2015a; Kang et al., 2016; Lüthi  
115 et al., 2015; Zhang et al., 2017). Cong et al. (2015b) suggested that strong large-scale  
116 westerly and local small-scale mountain-valley wind passed through western Nepal,  
117 northwest India and Pakistan (i.e., southern Himalayas) in the pre-monsoon season. Dumka et  
118 al. (2010) and Kang et al. (2016) inferred from the trajectory analysis that long-distance  
119 transport from Africa and Europe may also affect the BC concentration of Himalayas in  
120 addition to the influence of regional pollution. The synoptic troughs and ridges were also  
121 found favoring the transport of pollutants into the TP from South Asia (Lüthi et al., 2015).

122 Although previous studies have confirmed the transport of pollutants across the  
123 Himalayas, the complex topography of Himalayas complicates transport mechanisms. On one  
124 hand, Cao et al. (2010) revealed that the Himalayas acted as a huge barrier to the transport of  
125 a large amount of BC over the plateau based on model simulations. On the other hand, some  
126 studies found that the valleys across the Himalayas served as channels for efficient transport  
127 of pollutants (e.g., Hindman and Upadhyay, 2002; Marinoni et al., 2010). Marinoni et al.  
128 (2010) analyzed the observation of wind at a station of the southern Himalayas and found that  
129 a distinct valley wind system with the prominent southerly continuously transported  
130 pollutants to the plateau. Most of these studies used observations and back-trajectory models  
131 to demonstrate the transport pathways of pollutants to the TP, which cannot explicitly reveal  
132 the transport mechanisms underneath, in particular quantifying the impacts of complex  
133 topography.

134 A few of modeling studies investigated the pollutant transport mechanisms using 3-D  
135 chemical transport models (e.g., Kopacz et al., 2011; Liu et al., 2015; Zhang et al., 2017;  
136 Yang et al., 2018). However, most of them simulated transport processes at relatively coarse  
137 horizontal resolutions (e.g., 20-100 km), which cannot resolve well the complex topography  
138 of Himalayas. It is noteworthy that studies about the aerosol climatic impact over the TP also  
139 used climate models at relatively coarse horizontal resolutions (e.g., Flanner and Zender,  
140 2005; Menon et al., 2010; Kopacz et al., 2011; Qian et al., 2011, 2015; He et al., 2014; Zhang

141 et al., 2015; Ji et al., 2016). So far, there is only one study that used a chemical transport  
142 model at a horizontal resolution of sub-10 km to investigate pollutant transport mechanisms  
143 over the eastern Himalayas (Cao et al., 2010). Furthermore, none of studies assessed  
144 quantitatively the impacts of topography on modeling the pollutant transport across the  
145 Himalayas and hence on estimating aerosol distribution and radiative forcing over the TP.

146 In order to examine the potential impacts of complex topography on pollutant transport  
147 across the Himalayas over the TP, this study conducts multiple experiments with the Weather  
148 Research and Forecasting Model coupled with chemistry (WRF-Chem, Grell et al., 2005;  
149 Skamarock et al., 2008). The WRF-Chem model is selected because it includes the  
150 interaction between meteorology and aerosol and is widely used for regional modeling of  
151 aerosol and its climatic impact (e.g., Cao et al., 2010; Zhao et al., 2010, 2011, 2012, 2014;  
152 Wu et al., 2013; Gao et al., 2014; Huang et al., 2015; Fan et al., 2015; Feng et al., 2016;  
153 Zhong et al., 2017; Sarangi et al., 2019; Liu et al., 2020). The model has also been used to  
154 investigate the aerosol transport and climatic impact over the Himalayas region (e.g., Feng et  
155 al., 2016; Cao et al., 2010; Sarangi et al., 2019). The model is suitable for simulations at  
156 hydrostatic and non-hydrostatic scales and thus can be used for investigating the impacts of  
157 resolution-dependent feature, such as topography, on modeling results. In particular, the  
158 meteorological part of the model (WRF) has been systematically evaluated and used to  
159 investigate the impacts of resolutions on simulations of moisture transport and climate over  
160 the Himalayas region (e.g., Shi et al., 2008; Karki et al., 2017; Lin et al., 2018; Zhou et al.,  
161 2017, 2018; Wang et al., 2020). All of these previous studies with the model lay the  
162 foundation for this modeling study.

163 Two experiments with different topography representations are conducted to investigate  
164 the impacts of topography complexity on the pollutant transport across the Himalayas and the  
165 resulting radiative forcing over the TP. The simulations are conducted for April 2016 in  
166 pre-monsoon season, because South Asia is seriously polluted during this period and the  
167 pollutants transported to the TP during the period may have significant impacts on Asian  
168 monsoon system (e.g., Lau et al., 2006a, b; Ding et al., 2009; Kuhlmann and Quaas, 2010;  
169 Qian et al., 2011, 2015). In addition, the observed concentration of BC at the observation  
170 station besides Mt. Everest shows an evident pollution episode from April 5<sup>th</sup> to 16<sup>th</sup> of 2016,  
171 deserving the investigation of the transport mechanisms. The rest of the paper is organized as  
172 follows. Section 2 describes briefly the WRF-Chem model, the physics parameterizations,  
173 and the model configuration for this study, followed by a description of data for evaluation.

174 The series of numerical experiments at different resolutions are analyzed in Section 3. The  
175 findings are then summarized and discussed in Section 4 and 5.

176

## 177 **2. Methodology**

### 178 **2.1 Model and experiments**

#### 179 2.1.1 WRF-Chem model

180 In this study, the version of WRF-Chem updated by University of Science and  
181 Technology of China (USTC version of WRF-Chem) is used. This USTC version of  
182 WRF-Chem includes some additional capabilities such as the diagnosis of radiative forcing  
183 of aerosol species, land surface coupled biogenic volatile organic compound (VOC) emission,  
184 aerosol-snow interaction compared with the publicly released version (Zhao et al., 2013a, b,  
185 2014, 2016; Hu et al., 2019; Du et al., 2020). The Model for Simulating Aerosol Interactions  
186 and Chemistry (MOSIAC) (Zaveri et al., 2008) and the Carbon Bond Mechanism-Z (CBM-Z)  
187 gas phase mechanisms (Zaveri and Peters, 1999) are selected. The MOSAIC aerosol scheme  
188 uses an approach of segmentation to represent aerosol size distribution with four or eight  
189 discrete size bins (Fast et al., 2006). It consists of a range of physical and chemical processes  
190 such as nucleation, condensation, coagulation, aqueous phase chemistry, and water uptake by  
191 aerosol. The parameterization of dry deposition of aerosol mass and number is according to  
192 the method of Binkowski and Shankar (1995), including particle diffusion and gravitational  
193 effects. Aerosol-cloud interactions were included in the model by Gustafson et al. (2007) for  
194 calculating the activation and re-suspension between dry aerosols and cloud droplets. The wet  
195 removal of grid-resolved stratiform clouds/precipitation includes two aspects, namely  
196 in-cloud removal (rainout) and below-cloud removal (washout) by Easter et al. (2004) and  
197 Chapman et al. (2009), respectively. Aerosol optical properties such as single scattering  
198 albedo (SSA) and scattering asymmetry and so on are calculated at each model grid through  
199 the function of wavelength. The shortwave (SW) and longwave (LW) refractive indices of  
200 aerosols use the Optical Properties of Aerosols and Clouds (OPAC) data set (Hess et al.,  
201 1998), with a detailed description of the computation of aerosol optical properties can be  
202 found in Barnard et al. (2010) and Zhao et al. (2013a). For both short wave and long wave  
203 radiation, aerosol radiation feedback combined with the Rapid Radiative Transfer Model  
204 (RRTMG) (Mlawer et al., 1997; Iacono et al., 2000) was implemented by Zhao et al. (2011).  
205 For the diagnosis of the optical properties and direct radiative forcing of various aerosol  
206 species in the atmosphere, the method described by Zhao et al (2013a) is adopted. The

207 radiative forcing of light absorbing aerosol in surface snow is estimated with the Snow, Ice,  
208 and Aerosol Radiative model (SNICAR) (Flanner and Zender, 2005) in the land surface  
209 scheme as introduced by Zhao et al. (2014). More details about the coupling between the  
210 WRF-Chem and SNICAR models can be found in Zhao et al. (2014).

211

### 212 2.1.2 Numerical experiments

213 In this study, the WRF-Chem simulations are performed with two nested domains  
214 (one-way nesting), one outer domain at 20-km horizontal resolution with 350×250 grid cells  
215 (62°E -112°E, 1°N -38°N) and one inner domain at 4-km horizontal resolution with 400×300  
216 grid cells (75°E -92°E, 23°N -35°N) (Fig. 1). The inner domain roughly covers the entire  
217 Himalayas. The WRF-Chem simulations conducted in this study use the terrain following  
218 coordinate (Skamarock et al., 2008). To resolve the vertical structure of transport across the  
219 Himalayas, the simulations are configured with 54 vertical layers and denser layers near the  
220 surface. For example, averaged over a region (26°N-28°N, 76°E-80°E) near the southern  
221 Himalayas, there are about 17 layers below 2 km above the ground (Fig. 2). The goal of this  
222 study is to investigate the impacts of different representations of topography on the transport  
223 of BC across the Himalayas. Therefore, besides this control experiment, one sensitivity  
224 (idealized) experiment is also conducted with the same configuration as the control one  
225 except that the terrain ~~heights~~ of the inner domain at 4-km resolution ~~is prescribed to~~  
226 ~~follow that are bilinearly interpolated from the terrain heights~~ at 20-km resolution similar as  
227 previous studies (e.g., Shi et al., 2008; Wu et al., 2012b; Lin et al., 2018). ~~More specifically,~~  
228 ~~the sensitivity experiment applies a single value for each nested 5×5 grids over the inner~~  
229 ~~domain as the corresponding grid of 20 km over the outer domain.~~ The two experiments are  
230 referred to the simulations with complex and smooth topography, respectively, hereafter.

231 Fig. 3 shows the spatial distribution of terrain height over the inner domain with complex  
232 (4-km dataset) and smooth (20-km dataset) topography. It is evident that the terrain is much  
233 smoother from the 20-km dataset than from the 4-km dataset. The mountain ridges and  
234 valleys can be resolved to some extent in the 4-km dataset but mostly missed or  
235 underestimated at 20-km. The probability distributions of terrain height from the 20-km and  
236 4-km datasets (Fig. S1 in the supporting material) show that the difference between the two  
237 datasets is small for the terrain height lower than ~4.5 km but is significant for the terrain  
238 height above ~4.5 km. ~~In addition, the slopes between the neighboring grids are significantly~~  
239 ~~reduced in general with the smooth topography compared to with the complex topography.~~

240 [particularly over the Himalayas region \(Fig. S2 in the supporting material\)](#). The difference of  
241 results from the two experiments over the inner domain is analyzed as the impacts of  
242 topography representations. Therefore, all the results shown below are from the simulations  
243 of the inner domain at 4-km resolution with different topography if not otherwise stated. It is  
244 noteworthy that this study focuses on understanding the impact of complex topography  
245 resolved by 4 km instead of the difference between 4-km and 20-km simulations. Prescribing  
246 the topography at 4 km following the 20-km resolution distribution is just one way to smooth  
247 the topography. In fact, the sensitivity experiment at 4-km resolution with the topography  
248 from the one-degree resolution dataset is also conducted, and the result is consistent. In  
249 addition, although the topography at 4-km resolution resolves much better topography of  
250 Himalayas than that at 20-km resolution, it still cannot fully resolve the complexity of  
251 topography of Himalayas. The higher resolution (e.g., 1 km or sub-1 km) may be needed.  
252 Previous studies have found that the simulations at the resolutions between 1 km and 4 km  
253 can produce generally consistent features, but the simulation at 1 km with better  
254 representation of topography can produce a little better meteorological field compared to the  
255 observations (e.g., Karki et al., 2017). One sensitivity experiment at 1.5-km resolution is also  
256 conducted in this study and found the difference between the simulations at 1.5-km and 4-km  
257 resolutions is relatively small. However, it should be noted that the simulation at 1.5-km  
258 resolution is only conducted covering a much smaller region for a shorter period due to the  
259 computational cost. The experiment at 4-km instead of 1.5-km resolution is conducted finally  
260 for the study region and period due to the balance of resolving the complex topography to  
261 some extent and affordable computational cost.

262 The simulations are conducted for March 29th-April 20 of 2016 for the reason as  
263 discussed in the introduction. The results of April 1<sup>th</sup>-20<sup>th</sup> are analyzed for the observed  
264 pollution episode to allow a few days spin-up for chemical initial condition. The  
265 meteorological initial and lateral boundary conditions are derived from the European Centre  
266 for Medium-Range Weather Forecasts (ECMWF) reanalysis data at  $0.5^{\circ} \times 0.66^{\circ}$  horizontal  
267 resolution and 6 h temporal intervals (ERA-Interim dataset). The modeled u and v component  
268 wind, atmospheric temperature, and geopotential height over the outer domain are nudged  
269 towards the reanalysis data with a nudging timescale of 6 h following previous studies (e.g.,  
270 Stauffer and Seaman, 1990; Seaman et al., 1995; Liu et al., 2012; Zhao et al., 2014; Karki et  
271 al., 2017; Hu et al., 2016, 2020). Spectral nudging method is applied to balance the  
272 performance of simulation at the large and small scales (Liu et al., 2012), and only to the

273 layers above the planetary boundary layer (PBL) with nudging coefficients of  $3 \times 10^{-4} \text{ s}^{-1}$ . A  
274 wave number of three is selected for both south-north and west-east directions. Please note  
275 that the choices of nudging coefficients and wave numbers for spectral nudging in this study  
276 are empirical. The purpose of nudging is to simulate reasonably large-scale feature so that  
277 small-scale impacts from the complex topography can be focused. Therefore, the modeling  
278 sensitivity to these choices is not tested in this study. The results show that the simulations  
279 with nudging method can reproduce the large-scale circulation at 700 hPa and higher over the  
280 outer domain compared to the reanalysis dataset with the spatial correlation coefficient of  
281 0.96-0.98.

282 The Mellor-Yamada-Nakanishi-Niino (MYNN) planetary boundary layer scheme  
283 (Nakanishi and Niino, 2006), Community Land Model (CLM) land surface scheme (Oleson  
284 et al., 2010), Morrison 2-moment microphysics scheme (Morrison et al., 2009), Kain-Fritsch  
285 cumulus scheme (Kain, 2004), and Rapid Radiative Transfer Model (RRTMG) longwave and  
286 shortwave radiation schemes (Iacono et al., 2000) are used in this study. The chemical initial  
287 and boundary conditions are provided by a quasi-global WRF-Chem simulation for the same  
288 time period to include long-range transported chemical species. The quasi-global WRF-Chem  
289 simulation is performed at  $1^\circ \times 1^\circ$  horizontal resolution using a quasi-global channel  
290 configuration with  $360 \times 130$  grid cells ( $180^\circ\text{W}$ - $180^\circ\text{E}$ ,  $60^\circ\text{S}$ - $70^\circ\text{N}$ ). More details about the  
291 general configuration of quasi-global WRF-Chem simulation can be found in Zhao et al.  
292 (2013b) and Hu et al. (2016). The detailed configuration of WRF-Chem experiments is  
293 summarized in Table 1. Due to the lack of publicly available in-situ observations, this study  
294 does not tend to evaluate systematically the simulated meteorological fields over the  
295 Himalayas region. However, as shown in Table 1, the choice of physical parameterizations in  
296 this study follows that of one previous study (Karki et al., 2017) that evaluated systematically  
297 the WRF simulation for one entire year over the Himalayas region. Their results showed that  
298 the WRF simulation at convection-permitting scale could generally capture the essential  
299 features of meteorological fields such as precipitation, temperature, and wind over the  
300 Himalayas region. Therefore, the WRF-Chem simulations in this study are reliable to  
301 investigate the impacts of topography over the Himalayas region.

302

### 303 2.1.3 Emissions

304 Anthropogenic emissions for outer and inner simulation domains are obtained from the  
305 Hemispheric Transport of Air Pollution version-2 (HTAPv2) at  $0.1^\circ \times 0.1^\circ$  horizontal



306 resolution and a monthly temporal resolution for year 2010 (Janssens-Maenhout et al., 2015),  
307 except that emissions of East Asia are from the MIX Asian anthropogenic emission inventory  
308 at  $0.1^{\circ} \times 0.1^{\circ}$  horizontal resolution for 2015 (Li et al., 2017). Biomass burning emissions are  
309 obtained from the Fire Inventory from National Center for Atmospheric Research (FINN)  
310 with hourly temporal resolution and 1-km horizontal resolution (Wiedinmyer et al., 2011) for  
311 the simulation period, and are vertically distributed following the injection heights suggested  
312 by Dentener et al. (2006) from the Aerosol Comparison between Observations and Models  
313 (AeroCom) project. Sea-salt emission follows Zhao et al. (2013b), which includes correction  
314 of particles with radius less than  $0.2 \mu\text{m}$  (Gong, 2003) and dependence of sea-salt emission  
315 on sea surface temperature (Jaeglé et al., 2011). The vertical dust fluxes are calculated with  
316 the Georgia Tech/Goddard Global Ozone Chemistry Aerosol Radiation and Transport  
317 (GOCART) dust emission scheme (Ginoux et al., 2001), and the emitted dust particles are  
318 distributed into the MOSAIC aerosol size bins following a theoretical expression based on  
319 the physics of scale-invariant fragmentation of brittle materials derived by Kok (2011). More  
320 details about the dust emission scheme coupled with MOSAIC aerosol scheme in  
321 WRF-Chem can be found in Zhao et al. (2010, 2013b).

322 As shown in Fig. 1, anthropogenic fossil fuel emissions of BC are high over Northeast  
323 India. The fossil fuel BC emissions over Nepal, the country nearby the southern Himalayas,  
324 are relatively low. Instead, biomass burning emissions of BC are extremely high in Nepal and  
325 Northwest India (South Himalayas,  $26^{\circ}\text{N}$ - $29^{\circ}\text{N}$ ). Averaged over the South Himalayas of  
326 inner domain that may significantly affect the pollutant transport into the TP, the biomass  
327 burning emissions of BC are much higher than its anthropogenic fossil fuel emissions,  
328 particularly for the pollution episode (Fig. 4). The anthropogenic BC emissions are set  
329 constant through April, while biomass burning emissions show a strong fire event in April  
330 5-16. During the event, the biomass burning BC emissions can be a factor of 2 of the  
331 anthropogenic fossil fuel BC emissions over South Himalayas.

332

## 333 **2.2 Dataset**

334 Three datasets are used to compare with the modeling results to demonstrate the  
335 pollutant episode and spatial distribution. One is from the Moderate Resolution Imaging  
336 Spectroradiometer (MODIS) instruments on Aqua and Terra satellites. The MODIS Aerosol  
337 Product monitors the ambient aerosol optical thickness over the oceans globally and over the  
338 continents. Daily Level 2 Aerosol Optical Depth (AOD) at 550 nm products with the spatial  
339 resolution of  $10 \text{ km} \times 10 \text{ km}$  (at nadir) from both Aqua and Terra are applied. When compared

340 with the modeling results, the simulations are sampled at the satellite overpass time and  
341 location. The second one is from the Aerosol Robotic Network (AERONET) (Holben et al.,  
342 1998) that has ~100 similar globally distributed sun and sky scanning ground-based  
343 automated radiometers, which provide measurements of aerosol optical properties throughout  
344 the world (Dubovik and King, 2000; Dubovik et al., 2002). In this study, AERONET  
345 measured AOD at 675 nm and 440 nm from two sites over the TP, QOMS\_CAS site  
346 (86.95°E, 28.36°N) and NAM\_CO site (90.96°E, 30.77°N) are used to derive the AOD at  
347 550 nm (using the Angström exponent) for comparison with modeling results at 550 nm. All  
348 of the retrievals of AOD are at quality level 2, and the uncertainty of AOD measurements is  
349 about 0.01 (Holben et al., 2001). In this study, the available data in April 2016 are used to  
350 evaluate the modeling results during the same period.

351 The third one is the measurement of near-surface BC mass concentration collected  
352 during the simulation period for April 4-20 of 2016 at the Qomolangma Station for  
353 Atmospheric and Environmental Observation and Research (QOMS, 86.95°E, 28.36°N)  
354 which is located at the northern slope of the Mt. Everest, about 4276 meters above sea level.  
355 The BC mass concentration is measured with the widely-used instrument Aethalometer  
356 (AE-33) that can provide real-time BC mass concentration measurements. The calibration of  
357 air flow is routinely conducted to maintain the data quality. The instrument estimates the BC  
358 mass concentration based on the optical method through measuring the reduction in light  
359 intensity induced by BC. The method assumes that the relationship between attenuation and  
360 BC surface loading is linear for low attenuation values. However, this relationship becomes  
361 nonlinear when the attenuation values are high due to a filter saturation effect, which may  
362 lead to underestimation of the high BC concentration. The detection limit of AE-33  
363 instrument is 5 ng/m<sup>3</sup>, and the uncertainty is estimated to be within 10% (e.g., Chen et al.,  
364 2018; Bansal et al., 2019; Kant et al., 2019). The dataset of BC mass concentration used in  
365 this study was reported by Chen et al., (2018), where more details about the measurements  
366 can be found.

367

### 368 **3. Results**

#### 369 **3.1 Spatial distribution of BC around the TP**

370 Figure 5 shows the spatial distributions of column integrated BC mass within the inner  
371 domain from the simulations at 4-km resolution with complex and smooth topography  
372 averaged for April 1-20, 2016, and the difference between the two is also shown. For both

373 experiments, the Himalayas is an apparent boundary line for the distribution of BC with a  
374 sharp gradient across the Himalayas. The high BC mass loading exists near the southern  
375 Himalayas reaching over  $10 \text{ mg/m}^2$ , which is largely contributed by the biomass burning  
376 emissions during the period (Fig. 4), while the value reduces significantly to less than  $0.4$   
377  $\text{mg/m}^2$  over the TP. The BC mass loading near the central and eastern Himalayas is higher  
378 than that near the western Himalayas. In general, the column BC mass loading from the  
379 simulation with complex topography is higher over the TP and lower over the region to the  
380 south of Himalayas compared with the smooth topography, reflecting the stronger transport  
381 of BC from the source region to the Himalayas and TP due to the complex topography (see  
382 the discussion in Section 3.2). Figure 6 displays the spatial distributions of AOD from the  
383 MODIS retrievals and the simulations at 4 km with two different topography averaged for  
384 April 1-20, 2016. In general, both simulations reproduce the overall spatial distribution of  
385 AOD, with the large values near the southern Himalayas, consistent with the BC mass  
386 loading. In addition, both the simulations and satellite retrievals show higher AOD near the  
387 central and eastern Himalayas than that near the western Himalayas during the study period.  
388 The difference between the simulations and retrievals may be partly related to the  
389 uncertainties in emissions particularly for biomass burning emissions. Other than intense  
390 emissions, the wind circulation around the TP may also play an important role in  
391 accumulating BC near the southern Himalayas. Because of the block of Himalayas, the wind  
392 circulation at 500 hPa is divided into two branches as westerly and northwesterly. Both of  
393 them are relatively dry airflows with little effect on pollutant removal, favor the accumulation  
394 of pollutants near the southern Himalayas, and carry the pollutants to the TP (e.g., Dumka et  
395 al., 2010; Kang et al., 2016; Cong et al., 2015a).

396 The AOD retrieved at two AERONET sites over the TP are compared with the two  
397 simulations for April 1-20, 2016 (Fig. 7). The AOD at the QOMS\_CAS site near the northern  
398 Himalayas is higher than that at the NAM\_CO site inside of the TP. Both simulations can  
399 capture this gradient. The simulation with complex topography produces higher AOD than  
400 does the one with smooth topography at both sites. The modeling biases (normalized mean  
401 bias, NMB) reduce from -46% (smooth topography) to 9% (complex topography) at the  
402 QOMS\_CAS site and from -26% (smooth topography) to -10% (complex topography) at the  
403 NAM\_CO site. Although the correlation coefficient between the simulations and observation  
404 increases from 0.37 (smooth topography) to 0.53 (complex topography) at the QOMS\_CAS  
405 site, it is similar ( $\sim 0.2$ ) between the two simulations at the NAM\_CO site. The correlation  
406 coefficient is higher at the QOMS\_CAS site near the source region than the NAM\_CO site

407 farther away, which may indicate the model processes affecting the transport over the TP still  
408 need examination with more observations. The NAM\_CO site over the eastern TP may also  
409 be affected by other sources that are not counted in this study. The modeling of temporal  
410 variations of pollutants over the TP deserves further investigation with more observations.

411 There is one in-situ observational station (QOMS) near the Mt. Everest (black dot shown  
412 in Fig. 1) to collect the near-surface BC concentration. The observed near-surface BC  
413 concentration at this station is compared with the corresponding simulations for this period as  
414 shown in Figure 8. Without local emission source, the near-surface BC concentration at  
415 QOMS is primarily contributed by the transport. The temporal variation of observed  
416 near-surface BC concentration correlates highly with the biomass burning emissions as  
417 shown in Fig. 4, with the peak value on April 11 reaching  $\sim 3 \text{ ug/m}^3$ . One sensitivity  
418 experiment without biomass burning emissions shows that the simulated BC concentration at  
419 QOMS will be significantly reduced without the peak (not shown), which further proves that  
420 the BC concentration over the northern Himalayas can be largely influenced by the pollution  
421 episode near the southern Himalayas. It is noteworthy that both simulations can reproduce the  
422 episode in time and magnitude, and the difference at this station is small. The spatial  
423 distribution of difference in near-surface BC concentration between the two simulations (Fig.  
424 [S2S3](#)) is more heterogeneous than that of column BC mass (Fig. 5), reflecting the impact of  
425 topography on near-surface transport (see the discussion in Section 3.2).

426

### 427 **3.2 Transport flux into the TP**

428 To further understand the difference in BC near-surface concentration and column mass  
429 loading over the TP between the two simulations with different topography, Figure 9 shows  
430 the longitude-height cross section of BC transport flux along the cross line (shown as the  
431 black dash line in Fig. 3) from the two simulations at local time (LT) 03:00 and 15:00  
432 averaged for April 1-20 to represent nighttime and daytime transport, respectively. The PBL  
433 height along the cross line is also shown as the black dash line. The transport flux is  
434 calculated by projecting the wind field perpendicularly to the cross line and then multiplying  
435 the BC mass concentration along the cross line. More specifically, the transport flux is  
436 calculated as following:

$$437 \quad \text{TF} = C * (u * \sin \alpha + v * \sin \beta) \quad (1)$$

438 Where  $\alpha$  is the angle between east-west wind component and the cross line,  $\beta$  is the angle  
439 between south-north wind component and the cross line, and  $C$  is the BC mass

440 concentration at the grid along the cross line. The flux is estimated at each model level.  
441 Positive values represent the transport towards the TP, while negative values represent the  
442 transport away from the TP. It is evident that BC is imported into the TP during the day and  
443 night on the west of  $\sim 85^\circ\text{E}$ , although the transport flux is much larger during the daytime  
444 than nighttime. On the east of  $\sim 85^\circ\text{E}$ , BC is imported into the TP during the day but exported  
445 slightly from the TP during the night. The difference of transport flux between the western  
446 and eastern Himalayas is primarily due to the influence of large-scale westerly that is weak  
447 over the eastern Himalayas (Fig. 5). The transport across the western Himalayas is controlled  
448 by the large-scale westerly, while local southerly dominates the transport across the eastern  
449 Himalayas and also influences the transport across the central Himalayas (Fig. S3S4 in the  
450 supporting material). The stronger diurnal variation of local southerly (towards the TP in the  
451 daytime to away from the TP in the nighttime) than that of westerly near the surface (Fig.  
452 S3S4) leads to the large difference in diurnal variation of transport between the western and  
453 eastern Himalayas. The strong transport is primarily within the PBL during the daytime, and  
454 the deeper PBL during the daytime allows BC over the source region mixed to higher altitude,  
455 which also leads to stronger import transport during the day than the night. The relatively  
456 small difference in simulated PBL heights and structure between the two experiments can be  
457 due to their different surface heating resulted from different topography complexity (e.g.,  
458 Wagner et al., 2014).

459 The difference between the simulations with two different topography is evident. The  
460 mountain ridges are much higher and valleys are much deeper with the complex topography  
461 than with the smooth topography. The simulation with smooth topography produces  
462 overwhelming crossing-Himalayas transport towards the TP within the PBL, in particular  
463 during the daytime. Although, in the simulation with complex topography, the mountain  
464 ridges resolved weaken the crossing-Himalayas transport compared to the simulation with  
465 smooth topography, the overall positive values near the surface indicate that the transport can  
466 overcome most mountain ridges along the Himalayas. The transport fluxes near the surface  
467 from the simulation with complex topography become close-to-zero only at a few mountain  
468 ridges that are 6.5 km or higher. To better demonstrate the transport pathway across mountain  
469 ridges, one cross-section across the mountain ridge as shown as one black solid line in Fig. 3  
470 is taken as one example. Figure 10 shows the latitude-height cross section of BC mass  
471 concentration and transport flux across one mountain ridge from the simulations with  
472 complex and smooth topography at local time (LT) 03:00 and 15:00 averaged for April 1-20,  
473 2016. Near the southern part of mountain, the elevated concentration of BC mass

474 accumulates and can mix up reaching as high as 5 km with the much stronger transport  
 475 during the daytime. It is obvious that the mountain ridge in the simulation with smooth  
 476 topography is quite low. With the high mountain ridge resolved by the complex topography,  
 477 the simulated BC transport flux can still cross the mountain. Analysis of transport flux across  
 478 a few more mountain ridges indicates similar results (not shown). The results above indicate  
 479 that the transport of pollutants can cross a majority of mountain ridges of Himalayas, which  
 480 is consistent with the observation-based estimate by Gong et al. (2019) that also found  
 481 pollutants could overcome the blocking effect of mountain ridges of Himalayas as a transport  
 482 pathway. On the other hand, the resolved deeper valleys in the simulation with complex  
 483 topography enhance the transport flux compared to the one with the smooth topography.  
 484 Similarly, Figure 11 shows one example of latitude-height cross section of BC mass  
 485 concentration and transport flux across one valley from the simulations with complex and  
 486 smooth topography at local time (LT) 03:00 and 15:00 averaged for April 1-20, 2016. The  
 487 transport is much stronger and deeper along the valley from the simulation with complex  
 488 topography than the one with smooth topography. Again, analysis of transport flux across a  
 489 few more valleys does not show different results (not shown).

490 In order to further demonstrate the overall inflow flux across the Himalayas, the  
 491 vertically integrated BC mass flux along the longitudinal cross section (as shown in Fig. 9)  
 492 from the simulations with different topography is shown in Figure 12. The terrain heights  
 493 from the two simulations along the cross section are also shown as black lines. The total mass  
 494 flux is calculated by integrating the right-hand term of equation (1) as following:

$$495 \quad \text{ITF} = \int_{z=z_{sf c}}^{z=z_{top}} \delta z * C * (u * \sin \alpha + v * \sin \beta) \quad (2)$$

496 Where  $\delta z$  is the thickness of each vertical model level. Similarly, positive values represent  
 497 the transport towards the TP, while negative values represent the transport away from the TP.  
 498 More evidently, the positive BC inflows towards the TP occur not only through the valleys  
 499 but also across the mountain ridges with both topography. The negative values only exist to  
 500 the east of 88°E. With complex topography, higher mountain ridges can reduce the transport  
 501 flux to some extent compared to the smooth topography. The complex topography results in  
 502 significantly larger BC inflow towards the TP compared to the smooth topography,  
 503 particularly corresponding to the deep valleys, such as the Karnali River Valley around 82°E  
 504 and the Kali Gandaki Valley around 84°E.

505 One reason for the enhanced transport across the Himalayas with the complex  
 506 topography is the resolved deeper valleys that lead to the increased valley wind. The wind

507 across some valleys can be significantly larger with the complex topography than the smooth  
508 one (Fig. S3S4). The enhanced valley wind across the Himalayas has also been found by  
509 previous studies with observations and numerical simulations (e.g., Egger et al., 2000; Zängl  
510 et al., 2001; Carrera et al., 2009; Karki et al., 2017; Lin et al., 2018). However, it is  
511 noteworthy that previous studies have found that the orographic drag (including gravity wave  
512 drag and turbulence orographic form drag) over the region with complex topography, such as  
513 the Himalayas and other mountainous areas, would weaken the overall near-surface wind  
514 speed (e.g., Beljaars et al., 2004; Horvath et al., 2012; Jiménez and Dudhia, 2012; Zhou et al.,  
515 2017, 2018; Lin et al., 2018; Wang et al, 2020). Therefore, the near-surface wind speed is  
516 also examined. The complex topography does lead to the overall reduction of near-surface  
517 wind speed over the Himalayas area (Fig. S4S5 in the supporting material), which is  
518 consistent with previous studies. However, it is interesting to note that the near-surface  
519 southerly wind during the daytime of the simulation period is overall increased over the  
520 Himalayas area with the complex topography (Fig. 13), which indicates that the transport  
521 towards the TP is strengthened with the complex topography in the daytime, particularly over  
522 the central and eastern Himalayas where the BC mass loading is higher (Fig. 5). During the  
523 night, the meridional wind is dominated by northerly over the Himalayas region in the  
524 simulation with the smooth topography. The complex topography weakens the transport  
525 away from the TP or change the wind direction from northerly to southerly over some areas  
526 of Himalayas. Both effects enhance the overall transport efficiency across the Himalayas  
527 towards the TP. Therefore, although the complex topography weakens the overall  
528 near-surface wind speed around the Himalayas, it induces more realistic small-scale  
529 mountain-valley circulation that favors the BC transport across the Himalayas towards TP  
530 during the study period. Another effect of resolving valleys is that the volume of  
531 relatively-high-concentration BC could be higher with deeper valleys (Fig. S5S6 in the  
532 support material), which can also result in stronger transport towards the TP even if the wind  
533 condition is similar. For example, the altitude (above the ground) below which the BC mass  
534 concentration is larger than  $0.3\text{-}\mu\text{g}\cdot\text{m}^{-3}$  is much higher along the valleys with the complex  
535 topography than with the smooth topography (Fig. S6S7 in the support material). The  
536 correlation coefficient between the difference of terrain heights of valleys and of volumes of  
537 relatively-high-concentration BC can reach -0.76, indicating that the lower the valleys are,  
538 the higher the volumes of BC mass can be transported across the Himalayas. The combined  
539 influence of these factors results in significantly enhanced BC transport towards the TP with  
540 the complex topography (Fig. 12), which can also be demonstrated by the distributions of



541 wind and BC mass concentration along the longitudinal cross section (Fig. S7aS8a, b in the  
542 support material).

543 The enhanced transport across the Himalayas turns out that the overall BC inflow with  
544 the complex topography is much stronger than that with the smooth topography. Figure 14  
545 shows the accumulated integrated total transport flux of BC across the Himalayas estimated  
546 from the simulations with complex and smooth topography for April 1-20, 2016. The  
547 accumulated import flux of BC increases during the period in both experiments, and the  
548 difference between the two experiments gradually increases with the time. At the end of  
549 period, the simulation with complex topography estimates a total import flux of BC of  
550  $\sim 1.5 \times 10^4$  Ton that is  $\sim 50\%$  higher than  $\sim 1.0 \times 10^4$  Ton estimated based on the simulation with  
551 smooth topography. The sensitivity analysis by moving the cross line (cross-section of the  
552 analysis in Fig. 9, 12, 14) towards or away from the TP within a certain distance and  
553 re-calculating the flux indicates that the impacts of topography on the simulated results do  
554 not change significantly.

555 All the analysis above focuses on investigating the BC transport flux across the  
556 Himalayas. Although the inflow can reflect the impact of transport on the BC mass over the  
557 TP to some extent, the change of BC mass concentration is eventually determined by the  
558 convergence of transport. Therefore, the contribution of each model process (transport,  
559 dry-deposition, emission, PBL mixing, and wet deposition) to the increase of BC column  
560 mass averaged over the TP (with elevation  $> 4$  km) during this episode is analyzed for both  
561 simulations following the methodology introduced by Du et al. (2020). The results show that  
562 the two main processes affecting the BC column mass over the TP during the period are  
563 transport and dry deposition. The transport is the dominant process that increases the BC  
564 column mass over the TP, while the dry deposition reduces it. The contribution of transport to  
565 the increase of BC column mass over the TP during the episode from the simulation with  
566 complex topography is significantly larger than that with the smooth topography, which is  
567 consistent with the results shown by analyzing the transport flux across the Himalayas.  
568 Although the impacts of PBL mixing and wet deposition on the BC column mass over the TP  
569 are also different between the simulations with different topography, their impacts are much  
570 smaller than those of transport and dry deposition during the study period.

571

### 572 **3.3 Radiative forcing of BC over the TP**

573 The BC transported over the TP could significantly influence the regional climate and  
574 water resources over Asia through heating the atmosphere and accelerating the melting of  
575 snow and glacier (e.g., Qian et al., 2011, 2015; Lau et al., 2017). Therefore, the impact of the  
576 complex topography on estimating the BC radiative heating profile in the atmosphere and  
577 radiative forcing in surface snow deserves investigation. Figure 15 shows the vertical profiles  
578 of BC induced radiative heating rate in the atmosphere averaged over the TP (with  
579 elevation > 4 km) within the inner domain shown in Fig.1 for April 1-20, 2016 from the  
580 simulations with complex and smooth topography. Both simulations generate higher BC  
581 heating rate near the surface and the rate gradually decreases with altitude, which is  
582 consistent with the vertical profiles of BC mass concentration averaged over the TP (Fig.  
583 [S8S9](#) in the supporting material). The BC heating rate over the TP from the simulation with  
584 complex topography is ~0.17 K/day near the surface and reduces to ~0.08 K/day at 8 km,  
585 which is ~50% and ~30%, respectively, higher than that from the simulation with smooth  
586 topography at the corresponding altitudes. The higher BC heating rate over the TP estimated  
587 by the simulation with complex topography is consistent with its higher BC column mass  
588 (Fig. 5) and concentration profile (Fig. [S8S9](#)).

589 The BC radiative forcing in surface snow is controlled by both the distributions of BC  
590 mass concentration and snow coverage (e.g., Zhao et al., 2014). Figure 16 shows the spatial  
591 distributions of snow water equivalent (SWE) averaged for April 1-20, 2016 from the  
592 simulations with two topography. The difference between the two is also shown. It shows  
593 that the simulation with complex topography generates more areas with higher SWE  
594 compared to that with the smooth topography over the TP. Along the Himalayas, the  
595 simulated SWE is higher over the mountain ridges with the complex topography, particularly  
596 for the East Himalayas, while the smooth topography leads to broader snow coverage over  
597 the West Himalayas. The difference in SWE between the two simulations is highly correlated  
598 with their difference in precipitation (Fig. [S9S10](#) in the supporting material). Along the  
599 Himalayas, the simulated precipitation with the complex topography is larger than that with  
600 the smooth topography at the mountain ridges and smaller at the valleys. Over the TP, the  
601 overall precipitation is larger with the complex topography than that with the smooth  
602 topography (Fig. [S9S10](#)). Previous studies have found that the topography could significantly  
603 affect the precipitation over the Himalayas region (e.g., Bookhagen and Burbank, 2010; Wulf  
604 et al., 2016; Cannon et al., 2017; Karki et al., 2017).

605 Figure 17 shows the spatial distributions of BC radiative forcing in the surface snow  
606 over the TP averaged for April 1-20, 2016 from the simulations with two topography, and the

607 difference between the two is also shown. The BC radiative forcing in surface snow is largely  
608 coincident with the spatial distributions of SWE as shown in Fig. 16, mainly due to the  
609 heterogeneous distributions of snow cover over the TP. The BC radiative forcing in surface  
610 snow over the TP from the simulation with complex topography reaches  $5 \text{ W/m}^2$  where the  
611 snow exists, larger than that with the smooth topography. Along the Himalayas, the  
612 simulation with complex topography produces higher BC snow forcing over the mountain  
613 ridges, particularly over the eastern Himalayas, while the one with the smooth topography  
614 simulates higher BC snow forcing over most areas of western Himalayas due to its broader  
615 snow coverage there. Overall, the complex topography leads to higher BC forcing in snow  
616 over the TP and the eastern Himalayas and lower BC forcing in snow over the western  
617 Himalayas, and therefore results in the different distribution of BC forcing in snow over the  
618 TP and Himalayas, compared to that with the smooth topography.

619

620

621

#### 622 **4. Summary**

623 In this study, the model experiments with different topography are conducted to  
624 illustrate the impacts of complexity of topography of Himalayas on BC transport from South  
625 Asia to the TP. The observed pollution episode at the QOMS station besides the Mt. Everest  
626 during the pre-monsoon season is simulated. The observed near-surface BC concentration  
627 shows a peak of  $\sim 3 \text{ ug/m}^3$  much larger than the background value of  $< 0.4 \text{ ug/m}^3$  over the TP.  
628 The observed temporal variation of near-surface BC concentrations correlates highly with  
629 that of biomass burning emissions near the southern Himalayas, indicating the significant  
630 impacts of biomass burning on the pollutants over the TP. The simulations can reproduce the  
631 episode in time and magnitude, and are used to investigate the BC transport mechanisms and  
632 the impacts of topography.

633 The high BC mass loading during the simulation period accumulates near the southern  
634 Himalayas driven by the large-scale westerly and small-scale southerly circulations, which is  
635 also observed by satellites. The modeling results demonstrate that the circulations favor the  
636 accumulation of pollutants near the Himalayas, particularly over the central and eastern parts,  
637 and can carry the pollutants to the TP during the study period, which is consistent with  
638 previous modeling studies (e.g., Kopacz et al., 2011). It is noteworthy that the BC  
639 accumulated near the southern Himalayas can be transported across the Himalayas

640 overcoming a majority of mountain ridges, which is consistent with the observation-based  
641 estimate by Gong et al. (2019) that also found pollutants could overcome the blocking effect  
642 of the mountain ridges of Himalayas. However, the transport through the valleys is found  
643 much stronger and more efficient than across the mountain ridges and the enhancement effect  
644 cannot be ignored. The complex topography results in 50% higher overall transport flux  
645 across the Himalayas during the simulation period than that with the smooth topography,  
646 primarily due to the strengthened efficiency of near-surface meridional transport towards the  
647 TP, enhanced wind speed at some valleys, and deeper valley channels associated with larger  
648 BC mass volume that can be transported into the TP, although the overall wind speed is  
649 weakened due to the orographic drags with the complex topography. This turns out that the  
650 simulation with complex topography produces 30-50% higher BC radiative heating rate in  
651 the atmosphere up to 10 km averaged over the TP than does the simulation with smooth  
652 topography.

653 For the BC radiative forcing in surface snow, the simulation with complex topography  
654 produces stronger forcing over the TP than that with the smooth one. The complex  
655 topography makes the distribution of BC forcing in surface snow quite different from the  
656 simulation with smooth topography, partly due to its different distribution of surface snow.  
657 The simulated BC radiative forcing in snow is distributed more heterogeneously than those in  
658 previous studies using global models at relatively coarse resolutions (e.g., Qian et al., 2011).  
659 He et al. (2014) used a global chemical transport model to simulate the BC forcing in snow at  
660 the horizontal resolution of  $\sim 0.2^\circ$  and obtained the similar distribution as the simulation with  
661 smooth topography in this study with the high values over the western Himalayas. However,  
662 their simulated values near the Himalayas are higher than the simulated results of this study,  
663 which may be due to their estimation are averaged for November-April.

664 This study highlights the importance of resolving complex topography of the Himalayas  
665 in modeling the aerosol transport across the Himalayas and radiative impact over the TP.  
666 Although this study focuses on the impacts of topography on the simulated results, the  
667 additional analysis (Fig. [S10-12S11-13](#) in the supporting material) of the outer domain  
668 simulation at 20-km resolution and the inner domain simulation at 4 km with different  
669 topography indicates that the resolution-dependent difference between 20 km and 4 km is  
670 largely contributed by their different representations of topography over the Himalayas  
671 region, consistent with previous studies (e.g., Karki et al., 2017; Lin et al., 2018). Climate  
672 models at coarser horizontal resolutions than 20 km and thus with relatively smooth  
673 topography may underestimate the aerosol transport from South Asia to the TP during the

674 pre-monsoon season and represent inappropriately the aerosol radiative forcing in the  
675 atmosphere and surface snow over the TP.

676

## 677 **5. Discussion**

678 Previous studies also found the induced change of circulation and transport due to the  
679 complex topography at convection-permitting scales with the focus on the meteorological  
680 fields over the Himalayas and TP regions (e.g., Karki et al., 2017; Zhou et al., 2017, 2018;  
681 Lin et al., 2018; Wang et al., 2020). Most of them either conducted the sub-10 km  
682 simulations covering a relatively smaller region (e.g., 101×96 grids at 5 km in Karki et al.,  
683 2017; 181×121 grids at 2 km in Lin et al., 2018; ~330×230 grids at 3 km in Wang et al., 2020)  
684 compared to this study (400×300 grids at 4 km) or conducted the simulations covering the  
685 entire Himalayas but at the resolutions above 10 km and with the sub-grid  
686 orographic drag parameterization to consider the impact of complex topography. Although  
687 some of previous studies also showed that the resolved complex topography yielded more  
688 realistic small-scale mountain-valley circulations and enhanced valley winds over the  
689 Himalayas region compared to the smoother topography, the overall moisture transport  
690 across the Himalayas towards the TP was weaker with the complex topography due to the  
691 orographic drags.

692 The difference between previous studies and this study can be due to several factors.  
693 First, previous studies focused on moisture instead of air pollutants. The spatial (horizontal  
694 and vertical) distributions between air pollutants and moisture are different and may  
695 contribute to the different impacts of topography on the overall transport flux across the  
696 Himalayas. However, the analysis of the moisture from the simulations in this study shows  
697 the increase of moisture transport (not shown) and hence the increase of precipitation over  
698 the TP with the complex topography (Fig. [S9S10](#)). Second, most of previous studies focused  
699 on monsoon season instead of pre-monsoon season. Therefore, the meteorological  
700 simulations for monsoon season (June-July-August) at different resolutions are also  
701 conducted in this study. The results show that the moisture transport and precipitation are  
702 reduced at the higher resolution with complex topography and the meridional wind is overall  
703 weakened particularly over the central and eastern Himalayas and TP (not shown), which is  
704 consistent with previous studies. This may indicate that the different large-scale circulations  
705 between the two seasons (much stronger southerly during the monsoon season) may also lead

706 to different impacts of complex topography on meridional winds and hence cross-Himalayas  
707 transport.

708 Since this study only demonstrates the potential impacts for a relatively short period, a  
709 longer-term study should be conducted to examine the impacts of topography on aerosol  
710 climatic effect over the TP in both pre-monsoon and monsoon seasons. In addition, the active  
711 convection during the monsoon season may also play an important role on pollutant transport  
712 across the Himalayas, which deserves further investigation. Furthermore, aerosol impact on  
713 cloud and precipitation, particularly during the monsoon season, and thus on the latent heat in  
714 the atmosphere and the associated responses may also depend on the complex topography.  
715 Previous studies based on observations found that the rain frequency and intensity reached  
716 the highest and the cloud thickness reached the deepest at the foothill of Himalayas and  
717 decreased as the elevation increased up to the TP (e.g., Chen et al., 2017; Fu et al., 2018;  
718 Zhang et al., 2018), which was explained by Fu et al. (2018) due to the blocking of the air  
719 flow by the steep slope of southern Himalayas. However, the large amount of transported  
720 aerosol along the slope from the foothill up to the TP may also play a role. These potential  
721 impacts of aerosols on regional hydro-climate around the TP and over Asia using  
722 high-resolution model that can resolve the complex topography of Himalayas and TP deserve  
723 further investigation.

724

### 725 **Data availability**

726 The released version of WRF-Chem can be downloaded from  
727 [http://www2.mmm.ucar.edu/wrf/users/download/get\\_source.html](http://www2.mmm.ucar.edu/wrf/users/download/get_source.html). The updated USTC  
728 version of WRF-Chem can be downloaded from <http://aemol.ustc.edu.cn/product/list/> or  
729 contact [chunzhao@ustc.edu.cn](mailto:chunzhao@ustc.edu.cn). Also, the code modifications will be incorporated the  
730 release version of WRF-Chem in future.

731

### 732 **Author contributions**

733 Meixin Zhang and Chun Zhao designed the experiments, conducted and analyzed the  
734 simulations. All authors contributed to the discussion and final version of the paper.

735

### 736 **Acknowledgements**

737 This research was supported by the National Key Research and Development Program of  
738 China (2016YFA0602001), the National Natural Science Foundation of China NSFC (Grant

739 No. 91837310), the second Tibetan Plateau Scientific Expedition and Research Program  
740 (STEP) (2019QZKK0605), and the Fundamental Research Funds for the Central Universities.  
741 The study used computing resources from the High-Performance Computing Center of  
742 University of Science and Technology of China (USTC) and the TH-2 of National  
743 Supercomputer Center in Guangzhou (NSCC-GZ).  
744



745 **Reference**

- 750 Bansal, O., Singh, A., and Singh, D.: Characteristics of Black Carbon aerosols over Patiala  
751 Northwestern part of the IGP: Source apportionment using cluster and CWT analysis,  
752 Atmospheric Pollution Research, 10, 244–256, doi:10.1016/j.apr.2018.08.001, 2019.
- 753 Barnard, J. C., Fast, J. D., Paredes-Miranda, G., Arnott, W. P., and Laskin, A.: Technical  
754 Note: Evaluation of the WRF-Chem "Aerosol Chemical to Aerosol Optical Properties"  
755 Module using data from the MILAGRO campaign, Atmos. Chem. Phys., 10, 7325–7340,  
756 doi:10.5194/acp-10-7325-2010, 2010.
- 757 Beljaars, A. C., Brown, A. R., and Wood, N.: A new parametrization of turbulent orographic  
758 form drag, QJ Roy. Meteorol. Soc., 130, 1327–1347, doi: 10.1256/qj.03.73, 2004.
- 759 Barnett, T. P., Adam, J. C., and Lettenmaier, D. P.: Potential impacts of a warming climate  
760 on water availability in snow-dominated regions, Nature, 438, 303–309,  
761 doi:10.1038/nature04141, 2005.
- 762 Binkowski, F. S. and Shankar, U.: The Regional Particulate Matter Model: 1. Model  
763 description and preliminary results, J. Geophys. Res., 100, 26191, doi:10.1029/95JD02093,  
764 1995.
- 765 Bookhagen, B. and Burbank, D. W.: Toward a complete Himalayan hydrological budget:  
766 Spatiotemporal distribution of snowmelt and rainfall and their impact on river discharge, J.  
767 Geophys. Res., 115, 39, doi:10.1029/2009JF001426, 2010.
- 768 Boos, W. R. and Kuang, Z.: Sensitivity of the South Asian monsoon to elevated and  
769 non-elevated heating, Scientific reports, 3, 1192, doi:10.1038/srep01192, 2013.
- 770 Cannon, F., Carvalho, L. M. V., Jones, C., Norris, J., Bookhagen, B., and Kiladis, G. N.:  
771 Effects of topographic smoothing on the simulation of winter precipitation in High  
772 Mountain Asia, J. Geophys. Res. Atmos., 122, 1456–1474, doi:10.1002/2016JD026038,  
773 2017.
- 774 Cao, J., Tie, X., Xu, B., Zhao, Z., Zhu, C., Li, G., and Liu, S.: Measuring and modeling black  
775 carbon (BC) contamination in the SE Tibetan Plateau, Journal of Atmospheric Chemistry,  
776 67, 45–60, doi:10.1007/s10874-011-9202-5, 2010.
- 777 Carrera, M. L., Gyakum, J. R., and Lin, C. A.: Observational Study of Wind Channeling  
778 within the St. Lawrence River Valley, J. Appl. Meteorol. Clim., 48, 2341–2361,  
779 doi:10.1175/2009JAMC2061.1, 2009.
- 780 Chapman, E. G., Gustafson, W. I., Easter, R. C., Barnard, J. C., Ghan, S. J., Pekour, M. S.,  
781 and Fast, J. D.: Coupling aerosol-cloud-radiative processes in the WRF-Chem model:

782 Investigating the radiative impact of elevated point sources, *Atmos. Chem. Phys.*, 9,  
783 945–964, doi:10.5194/acp-9-945-2009, 2009.

784 Chen, J. and Bordoni, S.: Orographic Effects of the Tibetan Plateau on the East Asian  
785 Summer Monsoon: An Energetic Perspective, *J. Climate*, 27, 3052–3072,  
786 doi:10.1175/JCLI-D-13-00479.1, 2014.

787 Chen, X., Kang, S., Cong, Z., Yang, J., and Ma, Y.: Concentration, temporal variation, and  
788 sources of black carbon in the Mt. Everest region retrieved by real-time observation and  
789 simulation, *Atmos. Chem. Phys.*, 18, 12859–12875, doi:10.5194/acp-18-12859-2018,  
790 2018.

791 Chen, Y., Fu, Y., Xian, T., and Pan, X.: Characteristics of cloud cluster over the steep  
792 southern slopes of the Himalayas observed by CloudSat, *Int. J. Climatol.*, 37, 4043–4052,  
793 doi:10.1002/joc.4992, 2017.

794 Cong, Z., Kang, S., and Qin, D.: Seasonal features of aerosol particles recorded in snow from  
795 Mt. Qomolangma (Everest) and their environmental implications, *Journal of environmental  
796 sciences (China)*, 21, 914–919, doi:10.1016/S1001-0742(08)62361-X, 2009.

797 Cong, Z., Kang, S., Kawamura, K., Liu, B., Wan, X., Wang, Z., Gao, S., and Fu, P.:  
798 Carbonaceous aerosols on the south edge of the Tibetan Plateau: concentrations,  
799 seasonality and sources, *Atmos. Chem. Phys.*, 15, 1573–1584,  
800 doi:10.5194/acp-15-1573-2015, 2015a.

801 Cong, Z., Kawamura, K., Kang, S., and Fu, P.: Penetration of biomass-burning emissions  
802 from South Asia through the Himalayas: new insights from atmospheric organic acids,  
803 *Scientific reports*, 5, 9580, doi:10.1038/srep09580, 2015b.

804 Dentener, F., Kinne, S., Bond, T., Boucher, O., Cofala, J., Generoso, S., Ginoux, P., Gong, S.,  
805 Hoelzemann, J. J., Ito, A., Marelli, L., Penner, J. E., Putaud, J. P., Textor, C., Schulz, M.,  
806 van der Werf, G. R., and Wilson, J.: Emissions of primary aerosol and precursor gases in  
807 the years 2000 and 1750, prescribed data-sets for AeroCom, *Atmos. Chem. Phys.*, 6,  
808 4321–4344, doi:10.5194/acp-6-4321-2006, 2006.

809 Ding, Y., Sun, Y., Wang, Z., Zhu, Y., and Song, Y.: Inter-decadal variation of the summer  
810 precipitation in China and its association with decreasing Asian summer monsoon Part II:  
811 Possible causes, *Int. J. Climatol.*, 29, 1926–1944, doi:10.1002/joc.1759, 2009.

812 Du, Q., Zhao, C., Zhang, M., Dong, X., Chen, Y., Liu, Z., Hu, Z., Zhang, Q., Li, Y., Yuan, R.,  
813 , and Miao, S.: Modelling diurnal variation of surface PM<sub>2.5</sub> concentration over East  
814 China with WRF-Chem: Impacts from boundary layer mixing and anthropogenic

815 emission, *Atmos. Chem. Phys. Discuss.*, <https://doi.org/10.5194/acp-2019-739>, in review,  
816 2020.

817 Duan, A. M. and Wu, G. X.: Role of the Tibetan Plateau thermal forcing in the summer  
818 climate patterns over subtropical Asia, *Climate Dynamics*, 24, 793–807,  
819 doi:10.1007/s00382-004-0488-8, 2005.

820 Dubovik, O. and King, M. D.: A flexible inversion algorithm for retrieval of aerosol optical  
821 properties from Sun and sky radiance measurements, *J. Geophys. Res.*, 105, 20673–20696,  
822 doi:10.1029/2000JD900282, 2000.

823 Dubovik, O., Holben, B., Eck, T. F., Smirnov, A., Kaufman, Y. J., King, M. D., Tanré, D.,  
824 and Slutsker, I.: Variability of Absorption and Optical Properties of Key Aerosol Types  
825 Observed in Worldwide Locations, *J. Atmos. Sci.*, 59, 590–608,  
826 doi:10.1175/1520-0469(2002)059<0590:VOAAOP>2.0.CO;2, 2002.

827 Dumka, U. C., Moorthy, K. K., Kumar, R., Hegde, P., Sagar, R., Pant, P., Singh, N., and  
828 Babu, S. S.: Characteristics of aerosol black carbon mass concentration over a high altitude  
829 location in the Central Himalayas from multi-year measurements, *Atmospheric Research*,  
830 96, 510–521, doi:10.1016/j.atmosres.2009.12.010, 2010.

831 Easter, R. C., Ghan, S. J., Zhang, Y., Saylor, R. D., Chapman, E. G., Laulainen, N. S.,  
832 Abdul-Razzak, H., Leung, L. R., Bian, X., and Zaveri, R. A.: MIRAGE: Model  
833 Description and Evaluation of Aerosols and Trace Gases, *J. Geophys. Res.*, 109, D20210,  
834 doi:10.1029/2004JD004571, 2004.

835 Egger, J., Bajracharya, S., Egger, U., Heinrich, R., Reuder, J., Shakya, P., Wendt, H., and  
836 Wirth, V.: Diurnal winds in the Himalayan Kali Gandaki Valley. Part I: Observations, *Mon.*  
837 *Weather Rev.*, 128, 1106–1122, 2000.

838 Engling, G. and Gelencser, A.: Atmospheric Brown Clouds: From Local Air Pollution to  
839 Climate Change, *Elements*, 6, 223–228, doi:10.2113/gselements.6.4.223, 2010.

840 Fan, J., Rosenfeld, D., Yang, Y., Zhao, C., Leung, L. R., and Li, Z.: Substantial contribution  
841 of anthropogenic air pollution to catastrophic floods in Southwest China, *Geophys. Res.*  
842 *Lett.*, 42, 6066–6075, doi:10.1002/2015GL064479, 2015.

843 Fast, J. D., Gustafson Jr, W. I., Easter, R. C., Zaveri, R. A., Barnard, J. C., Chapman, E. G.,  
844 Grell, G. A., and Peckham, S. E.: Evolution of ozone, particulates, and aerosol direct  
845 radiative forcing in the vicinity of Houston using a fully coupled  
846 meteorology-chemistry-aerosol model, *J. Geophys. Res.*, 111, D21305,  
847 doi:10.1029/2005JD006721, 2006.

848 Feng, Y., Kotamarthi, V. R., Coulter, R., Zhao, C., and Cadeddu, M.: Radiative and  
849 thermodynamic responses to aerosol extinction profiles during the pre-monsoon month  
850 over South Asia, *Atmos. Chem. Phys.*, 16, 247–264, doi:10.5194/acp-16-247-2016, 2016.

851 Flanner, M. G. and Zender, C. S.: Snowpack radiative heating: Influence on Tibetan Plateau  
852 climate, *Geophys. Res. Lett.*, 32, L06501, doi:10.1029/2004GL022076, 2005.

853 Fu, Y., Pan, X., Xian, T., Liu, G., Zhong, L., Liu, Q., Li, R., Wang, Y., and Ma, M.:  
854 Precipitation characteristics over the steep slope of the Himalayas in rainy season observed  
855 by TRMM PR and VIRS, *Climate dynamics*, 51, 1971–1989,  
856 doi: 10.1007/s00382-017-3992-3, 2018.

857 Gao, Y., Zhao, C., Liu, X., Zhang, M., and Leung, L. R.: WRF-Chem simulations of aerosols  
858 and anthropogenic aerosol radiative forcing in East Asia, *Atmospheric Environment*, 92,  
859 250–266, doi:10.1016/j.atmosenv.2014.04.038, 2014.

860 Ginoux, P., Chin, M., Tegen, I., Prospero, J. M., Holben, B., Dubovik, O., and Lin, S.-J.:  
861 Sources and distributions of dust aerosols simulated with the GOCART model, *J. Geophys.*  
862 *Res.*, 106, 20255–20273, doi:10.1029/2000JD000053, 2001.

863 Gong, P., Wang, X., Pokhrel, B., Wang, H., Liu, X., Liu, X., and Wania, F.:  
864 Trans-Himalayan Transport of Organochlorine Compounds: Three-Year Observations and  
865 Model-Based Flux Estimation, *Environ. Sci. Technol.*, 53, 6773–6783,  
866 doi:10.1021/acs.est.9b01223, 2019.

867 Gong, S. L.: A parameterization of sea-salt aerosol source function for sub- and super-micron  
868 particles, *Global Biogeochem. Cycles*, 17, n/a-n/a, doi:10.1029/2003GB002079, 2003.

869 Grell, G. A., Peckham, S. E., Schmitz, R., McKeen, S. A., Frost, G., Skamarock, W. C., and  
870 Eder, B.: Fully coupled “online” chemistry within the WRF model, *Atmospheric*  
871 *Environment*, 39, 6957–6975, doi:10.1016/j.atmosenv.2005.04.027, 2005.

872 Gustafson, W. I., E. G. Chapman, S. J. Ghan, R. C. Easter, and J. D. Fast: Impact on modeled  
873 cloud characteristics due to simplified treatment of uniform cloud condensation nuclei  
874 during NEAQS 2004, *Geophys. Res. Lett.*, 34, L19809, doi:10.1029/2007GL030021,  
875 2007.

876 Hansen, J. and Nazarenko, L.: Soot climate forcing via snow and ice albedos, *Proceedings of*  
877 *the National Academy of Sciences*, 101, 423–428, doi:10.1073/pnas.2237157100, 2004.

878 He, C., Li, Q., Liou, K. N., Takano, Y., Gu, Y., Qi, L., Mao, Y., and Leung, L. R.: Black  
879 carbon radiative forcing over the Tibetan Plateau, *Geophys. Res. Lett.*, 41, 7806–7813,  
880 doi:10.1002/2014GL062191, 2014.

881 He, C., Wang, Z., Zhou, T., and Li, T.: Enhanced Latent Heating over the Tibetan Plateau as  
882 a Key to the Enhanced East Asian Summer Monsoon Circulation under a Warming  
883 Climate, *J. Climate*, 32, 3373–3388, doi:10.1175/JCLI-D-18-0427.1, 2019.

884 Hess, M., Koepke, P., and Schult, I.: Optical Properties of Aerosols and Clouds: The  
885 Software Package OPAC, *Bull. Amer. Meteor. Soc.*, 79, 831–844,  
886 doi:10.1175/1520-0477(1998)079<0831:OPOAAC>2.0.CO;2, 1998.

887 Hindman, E. E. and Upadhyay, B. P.: Air pollution transport in the Himalayas of Nepal and  
888 Tibet during the 1995–1996 dry season, *Atmospheric Environment*, 36, 727–739,  
889 doi:10.1016/S1352-2310(01)00495-2, 2002.

890 Holben, B. N., Eck, T. F., Slutsker, I., Tanré, D., Buis, J. P., Setzer, A., Vermote, E., Reagan,  
891 J. A., Kaufman, Y. J., Nakajima, T., Lavenu, F., Jankowiak, I., and Smirnov, A.:  
892 AERONET—A Federated Instrument Network and Data Archive for Aerosol  
893 Characterization, *Remote Sensing of Environment*, 66, 1–16,  
894 doi:10.1016/S0034-4257(98)00031-5, 1998.

895 Holben, B. N., Tanre, D., Smirnov, A., ECK T. F., Slutsker, I., Abuhassan, N., Newcomb, W.,  
896 Schafer, J., Chatenet, B., Lavenu, F., Kaufman, Y., Vande Castle, J., Setzer, A., Markham,  
897 B., Clark, D., Frouin, R., Halthore, R., Karneli, A., O'Neill, N., Pietras, C., Pinker, R.,  
898 Voss, K., and Zibordi, G.: An emerging ground-based aerosol climatology: Aerosol optical  
899 depth from AERONET, *J. Geophys. Res.*, 106, 12067-12097, doi:10.1029/2001JD900014,  
900 2001.

903 Horvath, K., Koracin, D., Vellore, R., Jiang, J., and Belu, R.: Sub - kilometer dynamical  
904 downscaling of near - surface winds in complex terrain using WRF and MM5 mesoscale  
905 models, *J. Geophys. Res. Atmos.*, 117, D11111, doi:10.1029/2012JD017432, 2012

906 Hu, Z., Huang, J., Zhao, C., Bi, J., Jin, Q., Qian, Y., Leung, L. R., Feng, T., Chen, S., and Ma,  
907 J.: Modeling the contributions of Northern Hemisphere dust sources to dust outflow from  
908 East Asia, *Atmospheric Environment*, 202, 234–243, doi:10.1016/j.atmosenv.2019.01.022,  
909 2019.

910 Hu, Z., Huang, J., Zhao, C., Jin, Q., Ma, Y., and Yang, B.: Modeling dust sources, transport,  
911 and radiative effects at different altitudes over the Tibetan Plateau, *Atmos. Chem. Phys.*  
912 *Discuss.*, <https://doi.org/10.5194/acp-2019-431>, in press, 2020.

913 Hu, Z., Zhao, C., Huang, J., Leung, L. R., Qian, Y., Yu, H., Huang, L., and Kalashnikova,  
914 O.V.: Trans-pacific transport and evolution of aerosols: Evaluation of quasi global

915 WRF-Chem simulation with multiple observations, *Geosci. Model Dev.*, 9, 1725–1746,  
916 doi:10.5194/gmd-9-1725-2016, 2016.

917 Huang, X., Song, Y., Zhao, C., Cai, X., Zhang, H., and Zhu, T.: Direct Radiative Effect by  
918 Multicomponent Aerosol over China, *J. Climate*, 28, 3472–3495,  
919 doi:10.1175/JCLI-D-14-00365.1, 2015.

920 Iacono, M. J., Mlawer, E. J., Clough, S. A., and Morcrette, J. J.: Impact of an improved  
921 longwave radiation model, RRTM, on the energy budget and thermodynamic properties of  
922 the NCAR community climate model, CCM3, *J. Geophys. Res.*, 105, 14873–14890,  
923 doi:10.1029/2000JD900091, 2000.

924 Immerzeel, W. W., van Beek, L. P. H., and Bierkens, M. F. P.: Climate change will affect the  
925 Asian water towers, *Science (New York, N.Y.)*, 328, 1382–1385,  
926 doi:10.1126/science.1183188, 2010.

927 Jaeglé, L., Quinn, P. K., Bates, T. S., Alexander, B., and Lin, J. T.: Global distribution of sea  
928 salt aerosols: new constraints from in situ and remote sensing observations, *Atmos. Chem.*  
929 *Phys.*, 11, 3137–3157, doi:10.5194/acp-11-3137-2011, 2011.

930 Janssens-Maenhout, G., Crippa, M., Guizzardi, D., Dentener, F., Muntean, M., Pouliot, G.,  
931 Keating, T., Zhang, Q., Kurokawa, J., Wankmüller, R., van der Denier Gon, H., Kuenen, J.  
932 J. P., Klimont, Z., Frost, G., Darras, S., Koffi, B., and Li, M.: HTAP\_v2.2: a mosaic of  
933 regional and global emission grid maps for 2008 and 2010 to study hemispheric transport  
934 of air pollution, *Atmos. Chem. Phys.*, 15, 11411–11432, doi:10.5194/acp-15-11411-2015,  
935 2015.

936 Ji, Z. M.: Modeling black carbon and its potential radiative effects over the Tibetan Plateau,  
937 *Advances in Climate Change Research*, 7, 139–144, doi:10.1016/j.accre.2016.10.002,  
938 2016.

939 Ji, Z., Kang, S., Cong, Z., Zhang, Q., and Yao, T.: Simulation of carbonaceous aerosols over  
940 the Third Pole and adjacent regions: distribution, transportation, deposition, and climatic  
941 effects, *Clim Dyn*, 45, 2831–2846, doi:10.1007/s00382-015-2509-1, 2015.

942 Jiménez, P. A. and Dudhia, J.: Improving the representation of resolved and unresolved  
943 topographic effects on surface wind in the WRF model, *J. Appl. Meteorol. Clim.*, 51,  
944 300–316, doi:10.1175/JAMC-D-11-084.1, 2012.

945 Kain, J. S.: The Kain–Fritsch Convective Parameterization: An Update, *J. Appl. Meteor.*, 43,  
946 170–181, doi:10.1175/1520-0450(2004)043<0170:TKCPAU>2.0.CO;2, 2004.

947 Kang, S, Chen P, Li C, Liu B, Cong Z: Atmospheric Aerosol Elements over the Inland  
948 Tibetan Plateau: Concentration, Seasonality, and Transport, *Aerosol Air Qual. Res.*, 16,  
949 789–800, doi:10.4209/aaqr.2015.02.0307, 2016.

950 Kang, S., Q. Zhang, Y. Qian, Z. Ji, C. Li, Z. Cong, Y. Zhang, J. Guo, W. Du, J. Huang, Q.  
951 You, A. K. Panday, M. Rupakheti, D. Chen, O. Gustafsson, M. H. Thiemens, and D. Qin:  
952 Linking atmospheric pollution to cryospheric change in the Third Pole region: current  
953 progress and future prospects, *National Science Review*, 6, 796–809,  
954 doi:10.1093/nsr/nwz031, 2019.

955 Kant, Y., Shaik, D. S., Mitra, D., Chandola, H. C., Babu, S. S., and Chauhan, P.: Black  
956 carbon aerosol quantification over north-west Himalayas: Seasonal heterogeneity, source  
957 apportionment and radiative forcing, *Environmental pollution (Barking, Essex 1987)*,  
958 113446, doi:10.1016/j.envpol.2019.113446, 2019.

959 Karki, R., ul Hasson, S., Gerlitz, L., Schickhoff, U., Scholten, T., and Böhner, J.: Quantifying  
960 the added value of convection-permitting climate simulations in complex terrain: a  
961 systematic evaluation of WRF over the Himalayas, *Earth Syst. Dynam.*, 8, 507–528,  
962 doi:10.5194/esd-8-507-2017, 2017.

963 Kok, J. F.: A scaling theory for the size distribution of emitted dust aerosols suggests climate  
964 models underestimate the size of the global dust cycle, *Proceedings of the National  
965 Academy of Sciences of the United States of America*, 108, 1016–1021,  
966 doi:10.1073/pnas.1014798108, 2011.

967 Kopacz, M., Mauzerall, D. L., Wang, J., Leibensperger, E. M., Henze, D. K., and Singh, K.:  
968 Origin and radiative forcing of black carbon transported to the Himalayas and Tibetan  
969 Plateau, *Atmos. Chem. Phys.*, 11, 2837–2852, doi:10.5194/acp-11-2837-2011, 2011.

970 Kuhlmann, J. and Quaas, J.: How can aerosols affect the Asian summer monsoon?  
971 Assessment during three consecutive pre-monsoon seasons from CALIPSO satellite data,  
972 *Atmos. Chem. Phys.*, 10, 4673–4688, doi:10.5194/acp-10-4673-2010, 2010.

973 Lau, K. M. and Kim, K. M.: Observational relationships between aerosol and Asian monsoon  
974 rainfall, and circulation, *Geophys. Res. Lett.*, 33, D22101, doi: 10.1029/2006GL027546,  
975 2006b.

976 Lau, K. M., Kim, M. K., and Kim, K. M.: Asian summer monsoon anomalies induced by  
977 aerosol direct forcing: the role of the Tibetan Plateau, *Clim Dyn*, 26, 855–864, doi:  
978 10.1007/s00382-006-0114-z, 2006a.

979 Lau, W. K. and Kim, K. M.: Impact of Snow Darkening by Deposition of Light-Absorbing  
980 Aerosols on Snow Cover in the Himalayas–Tibetan Plateau and Influence on the Asian

981 Summer Monsoon: A Possible Mechanism for the Blanford Hypothesis, *Atmosphere*, 9,  
 982 438, doi:10.3390/atmos9110438, 2018.

983 Lau, W. K. M., Kim, K. M., Shi, J. J., Matsui, T., Chin, M., Tan, Q., Peters-Lidard, C., and  
 984 Tao, W. K.: Impacts of aerosol–monsoon interaction on rainfall and circulation over  
 985 Northern India and the Himalaya Foothills, *Clim Dyn*, 49, 1945–1960,  
 986 doi:10.1007/s00382-016-3430-y, 2017.

987 Lau, W. K. M., Kim, M. K., Kim, K. M., and Lee, W. S.: Enhanced surface warming and  
 988 accelerated snow melt in the Himalayas and Tibetan Plateau induced by absorbing aerosols,  
 989 *Environ. Res. Lett.*, 5, 25204, doi:10.1088/1748-9326/5/2/025204, 2010.

990 Lee, W. S., Bhawar, R. L., Kim, M. K., and Sang, J.: Study of aerosol effect on accelerated  
 991 snow melting over the Tibetan Plateau during boreal spring, *Atmospheric Environment*, 75,  
 992 113–122, doi:10.1016/j.atmosenv.2013.04.004, 2013.

993 Li, C., Bosch, C., Kang, S., Andersson, A., Chen, P., Zhang, Q., Cong, Z., Chen, B., Qin, D.,  
 994 and Gustafsson, Ö.: Sources of black carbon to the Himalayan–Tibetan Plateau glaciers,  
 995 *Nat Commun*, 7, 4825, doi:10.1038/ncomms12574, 2016.

996 Li, M., Zhang, Q., Kurokawa, J. i., Woo, J. H., He, K., Lu, Z., Ohara, T., Song, Y., Streets, D.  
 997 G., Carmichael, G. R., Cheng, Y., Hong, C., Huo, H., Jiang, X., Kang, S., Liu, F., Su, H.,  
 998 and Zheng, B.: MIX: a mosaic Asian anthropogenic emission inventory under the  
 999 international collaboration framework of the MICS-Asia and HTAP, *Atmos. Chem. Phys.*,  
 1000 17, 935–963, doi:10.5194/acp-17-935-2017, 2017.

1001 Li, R. and Min, Q. L.: Impacts of mineral dust on the vertical structure of precipitation, *J.*  
 1002 *Geophys. Res.*, 115, 1337, doi:10.1029/2009JD011925, 2010.

1003 Li, R., Dong, X., Guo, J., Fu, Y., Zhao, C., Wang, Y., and Min, Q.: The implications of dust  
 1004 ice nuclei effect on cloud top temperature in a complex mesoscale convective system, *Sci*  
 1005 *Rep*, 7, 291, doi:10.1038/s41598-017-12681-0, 2017.

1006 Li, R., Shao, W., Guo, J., Fu, Y., Wang, Y., Liu, G., Zhou, R., and Li, W.: A Simplified  
 1007 Algorithm to Estimate Latent Heating Rate Using Vertical Rainfall Profiles Over the  
 1008 Tibetan Plateau, *J. Geophys. Res. Atmos.*, 124, 942–963, doi:10.1029/2018JD029297,  
 1009 2019.

1010 Lin, C., Chen, D., Yang, K., and Ou, T.: Impact of model resolution on simulating the water  
 1011 vapor transport through the central Himalayas: implication for models’ wet bias over the  
 1012 Tibetan Plateau, *Clim Dyn*, 51, 3195–3207, doi:10.1007/s00382-018-4074-x, 2018.



1013 Liu, P., Tsimpidi, A. P., Hu, Y., Stone, B., Russell, A. G., and Nenes, A.: Differences  
1014 between downscaling with spectral and grid nudging using WRF, *Atmos. Chem. Phys.*, 12,  
1015 3601–3610, doi:10.5194/acp-12-3601-2012, 2012.

1016 Liu, Y., Sato, Y., Jia, R., Xie, Y., Huang, J., and Nakajima, T.: Modeling study on the  
1017 transport of summer dust and anthropogenic aerosols over the Tibetan Plateau, *Atmos.*  
1018 *Chem. Phys.*, 15, 12581–12594, doi:10.5194/acp-15-12581-2015, 2015.

1019 Liu, Z., Ming, Y., Zhao, C., Lau, N. C., Guo, J., Bollasina, M., and Yim, S. H. L.:  
1020 Contribution of local and remote anthropogenic aerosols to a record-breaking torrential  
1021 rainfall event in Guangdong Province, China, *Atmos. Chem. Phys.*, 20, 223–241,  
1022 doi:10.5194/acp-20-223-2020, 2020.

1023 Lu, Z., Streets, D. G., Zhang, Q., and Wang, S.: A novel back-trajectory analysis of the origin  
1024 of black carbon transported to the Himalayas and Tibetan Plateau during 1996–2010,  
1025 *Geophys. Res. Lett.*, 39, n/a–n/a, doi:10.1029/2011GL049903, 2012.

1026 Lüthi, Z. L., Škerlak, B., Kim, S. W., Lauer, A., Mues, A., Rupakheti, M., and Kang, S.:  
1027 Atmospheric brown clouds reach the Tibetan Plateau by crossing the Himalayas, *Atmos.*  
1028 *Chem. Phys.*, 15, 6007–6021, doi:10.5194/acp-15-6007-2015, 2015.

1029 Lutz, A. F., Immerzeel, W. W., Shrestha, A. B., and Bierkens, M. F. P.: Consistent increase  
1030 in High Asia's runoff due to increasing glacier melt and precipitation, *Nature Clim Change*,  
1031 4, 587–592, doi:10.1038/nclimate2237, 2014.

1032 Marinoni, A., Cristofanelli, P., Laj, P., Duchi, R., Calzolari, F., Decesari, S., Sellegri, K.,  
1033 Vuillermoz, E., Verza, G. P., and Villani, P.: Aerosol mass and black carbon  
1034 concentrations, a two year record at NCO-P (5079 m, Southern Himalayas), *Atmos. Chem.*  
1035 *Phys.*, 10, 8551–8562, doi:10.5194/acp-10-8551-2010, 2010.

1036 Menon, S., Koch, D., Beig, G., Sahu, S., Fasullo, J., and Orlikowski, D.: Black carbon  
1037 aerosols and the third polar ice cap, *Atmos. Chem. Phys.*, 10, 4559–4571,  
1038 doi:10.5194/acp-10-4559-2010, 2010.

1039 Ming, J., Xiao, C., Cachier, H., Qin, D., Qin, X., Li, Z., and Pu, J.: Black Carbon (BC) in the  
1040 snow of glaciers in west China and its potential effects on albedos, *Atmospheric Research*,  
1041 92, 114–123, doi:10.1016/j.atmosres.2008.09.007, 2009.

1042 Mlawer, E. J., Taubman, S. J., Brown, P. D., Iacono, M. J., and Clough, S. A.: Radiative  
1043 transfer for inhomogeneous atmospheres: RRTM, a validated correlated-k model for the  
1044 longwave, *J. Geophys. Res.*, 102, 16663–16682, doi:10.1029/97JD00237, 1997.

1045 Morrison, H., Thompson, G., and Tatarskii, V.: Impact of Cloud Microphysics on the  
1046 Development of Trailing Stratiform Precipitation in a Simulated Squall Line: Comparison

1047 of One- and Two-Moment Schemes, *Mon. Wea. Rev.*, 137, 991–1007,  
1048 doi:10.1175/2008MWR2556.1, 2009.

1049 Nakanishi, M. and Niino, H.: An Improved Mellor–Yamada Level-3 Model: Its Numerical  
1050 Stability and Application to a Regional Prediction of Advection Fog, *Boundary-Layer*  
1051 *Meteorol*, 119, 397–407, doi:10.1007/s10546-005-9030-8, 2006.

1052 Oleson, K. W., Lawrence, D. M., Bonan, G. B., Flanner, M. G., Kluzek, E., Lawrence, P. J.,  
1053 Levis, S., Swenson, S. C., Thornton, P. E., Dai, A., Decker, M., Dickinson, R., Feddema, J.,  
1054 Heald, C. L., Hoffman, F., Lamarque, J. F., Mahowald, N., Niu, G. Y., Qian, T.,  
1055 Randerson, J., Running, S., Sakaguchi, K., Slater, A., Stockli, R., Wang, A., Yang, Z. L.,  
1056 Zeng, X., and Zeng, X.: Technical Description of version 4.0 of the Community Land  
1057 Model (CLM), Tech. Rep. NCAR/TN-478+STR, National Center for Atmospheric  
1058 Research, Boulder, Colorado, USA, 2010.

1059 Prasad, A. K. and Singh, R. P.: Comparison of MISR-MODIS aerosol optical depth over the  
1060 Indo-Gangetic basin during the winter and summer seasons (2000–2005), *Remote Sensing*  
1061 *of Environment*, 107, 109–119, doi:10.1016/j.rse.2006.09.026, 2007.

1062 Qian, Y., Flanner, M. G., Leung, L. R., and Wang, W.: Sensitivity studies on the impacts of  
1063 Tibetan Plateau snowpack pollution on the Asian hydrological cycle and monsoon climate,  
1064 *Atmos. Chem. Phys.*, 11, 1929–1948, doi:10.5194/acp-11-1929-2011, 2011.

1065 Qian, Y., Yasunari, T. J., Doherty, S. J., Flanner, M. G., Lau, W. K. M., Ming, J., Wang, H.,  
1066 Wang, M., Warren, S. G., and Zhang, R.: Light-absorbing particles in snow and ice:  
1067 Measurement and modeling of climatic and hydrological impact, *Adv. Atmos. Sci.*, 32,  
1068 64–91, doi:10.1007/s00376-014-0010-0, 2015.

1069 Qiu, J.: China: The third pole, *Nature*, 454, 393–396, doi:10.1038/454393a, 2008.

1070 Ramanathan, V. and Carmichael, G.: Global and regional climate changes due to black  
1071 carbon, *Nature Geosci*, 1, 221–227, doi:10.1038/ngeo156, 2008.

1072 Ramanathan, V., Ramana, M. V., Roberts, G., Kim, D., Corrigan, C., Chung, C., and Winker,  
1073 D.: Warming trends in Asia amplified by brown cloud solar absorption, *Nature*, 448,  
1074 575–578, doi:10.1038/nature06019, 2007.

1075 Sarangi, C., Qian, Y., Rittger, K., Bormann, K. J., Liu, Y., Wang, H., Lin, G., and Painter, T.  
1076 H.: Impact of light-absorbing particles on snow albedo darkening and associated radiative  
1077 forcing over high-mountain Asia: high-resolution WRF-Chem modeling and new satellite  
1078 observations. *Atmos. Chem. Phys.*, 19, 7105–7128, doi:10.5194/acp-19-7105-2019, 2019.

1079 Seaman, N. L., Stauffer, D. R., and Lario-Gibbs, A. M.: A Multiscale Four-Dimensional Data  
1080 Assimilation System Applied in the San Joaquin Valley during SARMAP. Part I:

1081 Modeling Design and Basic Performance Characteristics, *J. Appl. Meteor.*, 34, 1739–1761,  
1082 doi:10.1175/1520-0450(1995)034<1739:AMFDDA>2.0.CO;2, 1995.

1083 Shi, X., Wang, Y., and Xu, X.: Effect of mesoscale topography over the Tibetan Plateau on  
1084 summer precipitation in China: A regional model study, *Geophys. Res. Lett.*, 35, 255,  
1085 doi:10.1029/2008GL034740, 2008.

1086 Singh, P. and Bengtsson, L.: Hydrological sensitivity of a large Himalayan basin to climate  
1087 change, *Hydrol. Process.*, 18, 2363–2385, doi:10.1002/hyp.1468, 2004.

1088 Skamarock, W. C., Klemp, J. B., Dudhia, J., Gill, D. O., Barker, D. M., Duda, M., Huang, X.  
1089 Y., Wang, W., and Powers, J. G.: A Description of the Advanced Research WRF Version 3,  
1090 NCAR Technical Note, NCAR/TN-468+STR, available at:  
1091 [http://wrf-model.org/wrfadmin/docs/arw\\_v2.pdf](http://wrf-model.org/wrfadmin/docs/arw_v2.pdf), 2008.

1092 Stauffer, D. R. and Seaman, N. L.: Use of Four-Dimensional Data Assimilation in a  
1093 Limited-Area Mesoscale Model. Part I: Experiments with Synoptic-Scale Data, *Mon. Wea.*  
1094 *Rev.*, 118, 1250–1277, doi:10.1175/1520-0493(1990)118<1250:UOFDDA>2.0.CO;2,  
1095 1990.

1096 Wagner, J. S., Gohm, A., and Rotach, M. W.: The Impact of Horizontal Model Grid  
1097 Resolution on the Boundary Layer Structure over an Idealized Valley, *Mon. Wea. Rev.*,  
1098 142, 3446–3465, doi:10.1175/MWR-D-14-00002.1, 2014.

1099 Wang, X., Gong, P., Sheng, J., Joswiak, D. R., and Yao, T.: Long-range atmospheric  
1100 transport of particulate Polycyclic Aromatic Hydrocarbons and the incursion of aerosols to  
1101 the southeast Tibetan Plateau, *Atmospheric Environment*, 115, 124–131,  
1102 doi:10.1016/j.atmosenv.2015.04.050, 2015.

1103 Wang, Y., Yang, K., Zhou, X., Chen, D., Lu, H., Ouyang, L., Chen, Y., Lazhu., and Wang,  
1104 B.: Synergy of orographic drag parameterization and high resolution greatly reduces biases  
1105 of WRF-simulated precipitation in central Himalaya, *Climate Dynamics*, 54, 1729–1740,  
1106 doi:10.1007/s00382-019-05080-w, 2020.

1107 Wiedinmyer, C., Akagi, S. K., Yokelson, R. J., Emmons, L. K., Al-Saadi, J. A., Orlando, J. J.,  
1108 and Soja, A. J.: The Fire INventory from NCAR (FINN): a high resolution global model to  
1109 estimate the emissions from open burning, *Geosci. Model Dev.*, 4, 625–641,  
1110 doi:10.5194/gmd-4-625-2011, 2011.

1111 Wu, G., Liu, Y., Dong, B., Liang, X., Duan, A., Bao, Q., and Yu, J.: Revisiting Asian  
1112 monsoon formation and change associated with Tibetan Plateau forcing: I. Formation,  
1113 *Clim Dyn*, 39, 1169–1181, doi:10.1007/s00382-012-1334-z, 2012a.

- 1114 Wu, G., Liu, Y., He, B., Bao, Q., Duan, A., and Jin, F. F.: Thermal controls on the Asian  
1115 summer monsoon, *Scientific reports*, 2, 404, doi:10.1038/srep00404, 2012b.
- 1116 Wu, G., Liu, Y., Zhang, Q., Duan, A., Wang, T., Wan, R., Liu, X., Li, W., Wang, Z., and  
1117 Liang, X.: The Influence of Mechanical and Thermal Forcing by the Tibetan Plateau on  
1118 Asian Climate, *J. Hydrometeor.*, 8, 770–789, doi:10.1175/JHM609.1, 2007.
- 1119 Wu, L., Su, H., and Jiang, J. H.: Regional simulation of aerosol impacts on precipitation  
1120 during the East Asian summer monsoon, *J. Geophys. Res. Atmos.*, 118, 6454–6467,  
1121 doi:10.1002/jgrd.50527, 2013.
- 1122 Wulf, H., Bookhagen, B., and Scherler, D.: Differentiating between rain, snow, and glacier  
1123 contributions to river discharge in the western Himalaya using remote-sensing data and  
1124 distributed hydrological modeling, *Advances in Water Resources*, 88, 152–169,  
1125 doi:10.1016/j.advwatres.2015.12.004, 2016.
- 1126 Yang, J., Kang, S., Ji, Z., and Chen, D.: Modeling the Origin of Anthropogenic Black Carbon  
1127 and Its Climatic Effect Over the Tibetan Plateau and Surrounding Regions, *J. Geophys.*  
1128 *Res. Atmos.*, 123, 671–692, doi:10.1002/2017JD027282, 2018.
- 1129 Yasunari, T. J., Bonasoni, P., Laj, P., Fujita, K., Vuillermoz, E., Marinoni, A., Cristofanelli,  
1130 P., Duchi, R., Tartari, G., and Lau, K.-M.: Estimated impact of black carbon deposition  
1131 during pre-monsoon season from Nepal Climate Observatory – Pyramid data and snow  
1132 albedo changes over Himalayan glaciers, *Atmos. Chem. Phys.*, 10, 6603–6615,  
1133 doi:10.5194/acp-10-6603-2010, 2010.
- 1134 Ye, D. Z. and Wu, G. X.: The role of the heat source of the Tibetan Plateau in the general  
1135 circulation, *Meteorol. Atmos. Phys.*, 67, 181–198, doi:10.1007/BF01277509, 1998.
- 1136 Zängl, G., Egger, J., and Wirth, V.: Diurnal Winds in the Himalayan Kali Gandaki Valley.  
1137 Part II: Modeling, *Mon. Wea. Rev.*, 129, 1062–1080,  
1138 doi:10.1175/1520-0493(2001)129<1062:DWITHK>2.0.CO;2, 2001.
- 1139 Zaveri, R. A. and Peters, L. K.: A new lumped structure photochemical mechanism for  
1140 large-scale applications, *J. Geophys. Res.*, 104, 30387–30415, doi:10.1029/1999JD900876,  
1141 1999.
- 1142 Zaveri, R. A., Easter, R. C., Fast, J. D., and Peters, L. K.: Model for Simulating Aerosol  
1143 Interactions and Chemistry (MOSAIC), *J. Geophys. Res.*, 113, 1591,  
1144 doi:10.1029/2007JD008782, 2008.
- 1145 Zhang, A., Fu, Y., Chen, Y., Liu, G., and Zhang, X.: Impact of the surface wind flow on  
1146 precipitation characteristics over the southern Himalayas: GPM observations, *Atmospheric*  
1147 *Research*, 202, 10–22, doi:10.1016/j.atmosres.2017.11.001, 2018.

1148 Zhang, R., Wang, H., Qian, Y., Rasch, P. J., Easter, R. C., Ma, P. L., Singh, B., Huang, J.,  
1149 and Fu, Q.: Quantifying sources, transport, deposition, and radiative forcing of black  
1150 carbon over the Himalayas and Tibetan Plateau, *Atmos. Chem. Phys.*, 15, 6205–6223,  
1151 doi:10.5194/acp-15-6205-2015, 2015.

1152 Zhang, R., Wang, Y., He, Q., Chen, L., Zhang, Y., Qu, H., Smeltzer, C., Li, J., Alvarado, L.  
1153 M. A., Vrekoussis, M., Richter, A., Wittrock, F., and Burrows, J. P.: Enhanced  
1154 trans-Himalaya pollution transport to the Tibetan Plateau by cut-off low systems, *Atmos.*  
1155 *Chem. Phys.*, 17, 3083–3095, doi:10.5194/acp-17-3083-2017, 2017.

1156 Zhang, Y., Kang, S., Cong, Z., Schmale, J., Sprenger, M., Li, C., Yang, W., Gao, T.,  
1157 Sillanpää, M., Li, X., Liu, Y., Chen, P., and Zhang, X.: Light-absorbing impurities enhance  
1158 glacier albedo reduction in the southeastern Tibetan plateau, *J. Geophys. Res. Atmos.*, 122,  
1159 6915–6933, doi:10.1002/2016JD026397, 2017.

1160 Zhang, Y., Kang, S., Sprenger, M., Cong, Z., Gao, T., Li, C., Tao, S., Li, X., Zhong, X., Xu,  
1161 M., Meng, W., Neupane, B., Qin, X., and Sillanpää, M.: Black carbon and mineral dust in  
1162 snow cover on the Tibetan Plateau, *The Cryosphere*, 12, 413–431,  
1163 doi:10.5194/tc-12-413-2018, 2018.

1164 Zhao, C., Chen, S., Leung, L. R., Qian, Y., Kok, J., Zaveri, R., and Huang, J.: Uncertainty in  
1165 modeling dust mass balance and radiative forcing from size parameterization, *Atmos.*  
1166 *Chem. Phys.*, 13, 10733–10753, doi:doi:10.5194/acp-13-10733-2013, 2013b.

1167 Zhao, C., Hu, Z., Qian, Y., Leung, L. R., Huang, J., Huang, M., Jin, J., Flanner, M., Zhang,  
1168 R., Wang, H., Yan, H., Lu, Z., and Streets, D. G.: Simulating black carbon and dust and  
1169 their radiative forcing in seasonal snow: a case study over North China with field  
1170 campaign measurements, *Atmos. Chem. Phys.*, 14, 11475–11491,  
1171 doi:10.5194/acp-14-11475-2014, 2014.

1172 Zhao, C., Huang, M., Fast, J. D., Berg, L. K., Qian, Y., Guenther, A., Gu, D., Shrivastava, M.,  
1173 Liu, Y., and Walters, S.: Sensitivity of biogenic volatile organic compounds to land surface  
1174 parameterizations and vegetation distributions in California, *Geosci. Model Dev*, 9,  
1175 1959–1976, doi:10.5194/gmd-9-1959-2016, 2016.

1176 Zhao, C., Liu, X., and Leung, L. R.: Impact of the Desert dust on the summer monsoon  
1177 system over Southwestern North America, *Atmos. Chem. Phys.*, 12, 3717–3731,  
1178 doi:10.5194/acp-12-3717-2012, 2012.

1179 Zhao, C., Liu, X., Leung, L. R., and Hagos, S.: Radiative impact of mineral dust on monsoon  
1180 precipitation variability over West Africa, *Atmos. Chem. Phys.*, 11, 1879–1893,  
1181 doi:10.5194/acp-11-1879-2011, 2011.

1182 Zhao, C., Liu, X., Leung, L. R., Johnson, B., McFarlane, S. A., Gustafson, W. I., Fast, J. D.,  
1183 and Easter, R.: The spatial distribution of mineral dust and its shortwave radiative forcing  
1184 over North Africa: modeling sensitivities to dust emissions and aerosol size treatments,  
1185 *Atmos. Chem. Phys.*, 10, 8821–8838, doi:10.5194/acp-10-8821-2010, 2010.

1186 Zhao, C., Ruby Leung, L., Easter, R., Hand, J., and Avise, J.: Characterization of speciated  
1187 aerosol direct radiative forcing over California, *J. Geophys. Res. Atmos.*, 118, 2372–2388,  
1188 doi:10.1029/2012JD018364, 2013a.

1189 Zhao, P., Zhou, X., Chen, J., Liu, G., and Nan, S.: Global climate effects of summer Tibetan  
1190 Plateau, *Science Bulletin*, 64, 1–3, doi:10.1016/j.scib.2018.11.019, 2019.

1191 Zhou, X., Beljaars, A., Wang, Y., Huang, B., Lin, C., Chen, Y., and Wu, H.: Evaluation of  
1192 WRF simulations with different selections of subgrid orographic drag over the Tibetan  
1193 Plateau, *J. Geophys. Res. Atmos.*, 122, 9759–9772, doi:10.1002/2017JD027212, 2017.

1194 Zhou, X., Yang, K., and Wang, Y.: Implementation of a turbulent orographic form drag  
1195 scheme in WRF and its application to the Tibetan Plateau, *Climate dynamics*, 50,  
1196 2443–2455, doi: 10.1007/s00382-017-3677-y, 2018.

1197 Zhao, Z., Cao, J., Shen, Z., Xu, B., Zhu, C., Chen, L. W. A., Su, X., Liu, S., Han, Y., Wang,  
1198 G., and Ho, K.: Aerosol particles at a high-altitude site on the Southeast Tibetan Plateau,  
1199 China: Implications for pollution transport from South Asia, *J. Geophys. Res. Atmos.*, 118,  
1200 11,360–11,375, doi:10.1002/jgrd.50599, 2013.

1201 Zhong, S., Qian, Y., Zhao, C., Leung, R., Wang, H., Yang, B., Fan, Ji., Yan, H., Yang, X.,  
1202 and Liu, D.: Urbanization-induced urban heat island and aerosol effects on climate  
1203 extremes in the Yangtze River Delta region of China, *Atmos. Chem. Phys.*, 17, 5439–5457,  
1204 doi:10.5194/acp-17-5439-2017, 2017.

1205  
1206  
1207  
1208  
1209  
1210  
1211  
1212  
1213  
1214  
1215  
1216  
1217  
1218

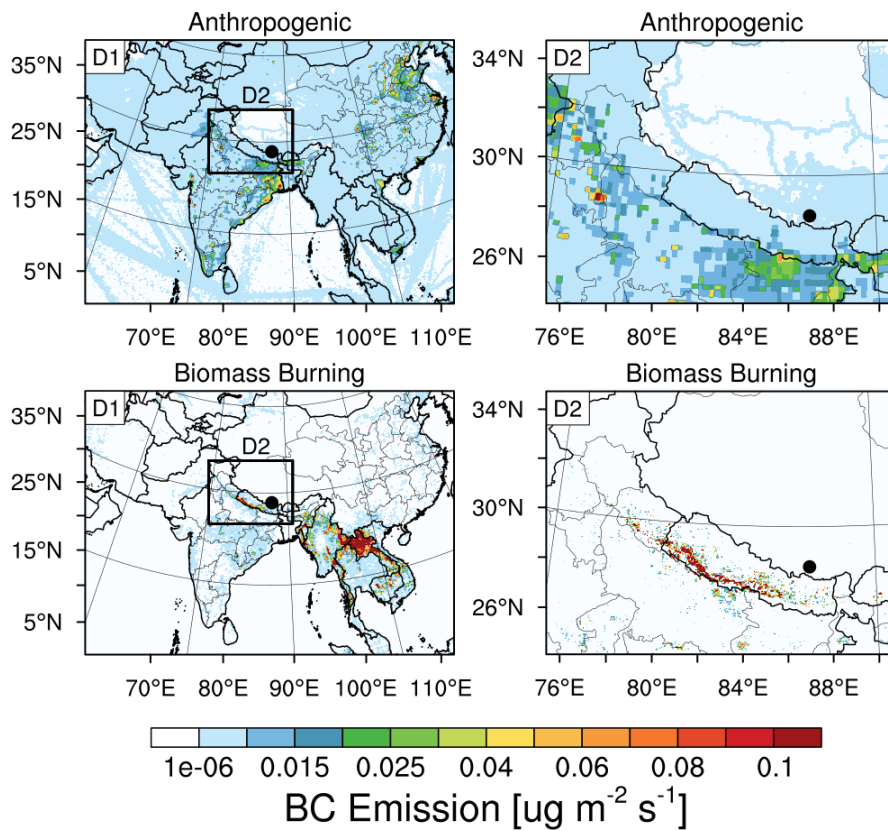
1219  
 1220  
 1221  
 1222  
 1223  
 1224  
 1225  
 1226  
 1227  
 1228  
 1229  
 1230

**Table 1.** Summary of model configurations.

<b>Description</b>	<b>Selection</b>	<b>References</b>
<b>Horizontal grid spacing</b>	20 km (D1), 4 km (D2)	
<b>Grid dimensions</b>	250×350, 300×400	
<b>Topography</b>	30 arcsec (USGS)	
<b>Vertical layers</b>	54 (roughly 17 layers below 2 km)	
<b>Model top pressure</b>	50 hPa	
<b>Nesting approach</b>	One-way	
<b>Aerosol scheme</b>	MOSAIC 8 bin	Zaveri et al., 2008
<b>Gas-phase chemistry</b>	CBM-Z	Zaveri and Peters, 1999
<b>Long wave Radiation</b>	RRTMG	Iacono et al., 2000; Zhao et al., 2011, 2013a
<b>Short-wave Radiation</b>	RRTMG	
<b>Cloud Microphysics</b>	Morrison 2-moment	Morrison et al., 2009
<b>Cumulus Cloud</b>	Kain-Fritsch	Kain, 2004
<b>Planetary boundary layer</b>	MYNN level 2.5	Nakanishi and Niino, 2006
<b>Land surface</b>	CLM	Oleson et al., 2010
<b>Meteorological Forcing</b>	ERA-Interim, 0.5°×0.66°, 6 hourly	

1231  
 1232  
 1233  
 1234  
 1235  
 1236  
 1237  
 1238  
 1239  
 1240  
 1241  
 1242  
 1243  
 1244  
 1245  
 1246  
 1247  
 1248

1249  
1250  
1251  
1252  
1253  
1254  
1255  
1256  
1257  
1258  
1259  
1260  
1261

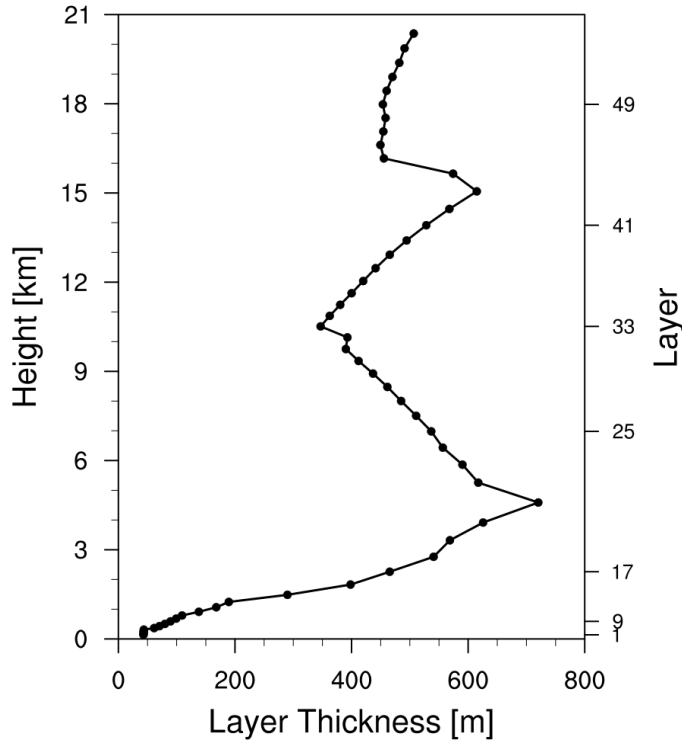


1262  
1263  
1264  
1265  
1266  
1267  
1268  
1269  
1270  
1271  
1272  
1273  
1274  
1275  
1276  
1277

**Figure 1.** Anthropogenic and fire emissions over the entire simulated regions of 20-km and 4-km resolutions, the black dot represents the Qomolangma Station (QOMS, 86.95°E, 28.36°N).



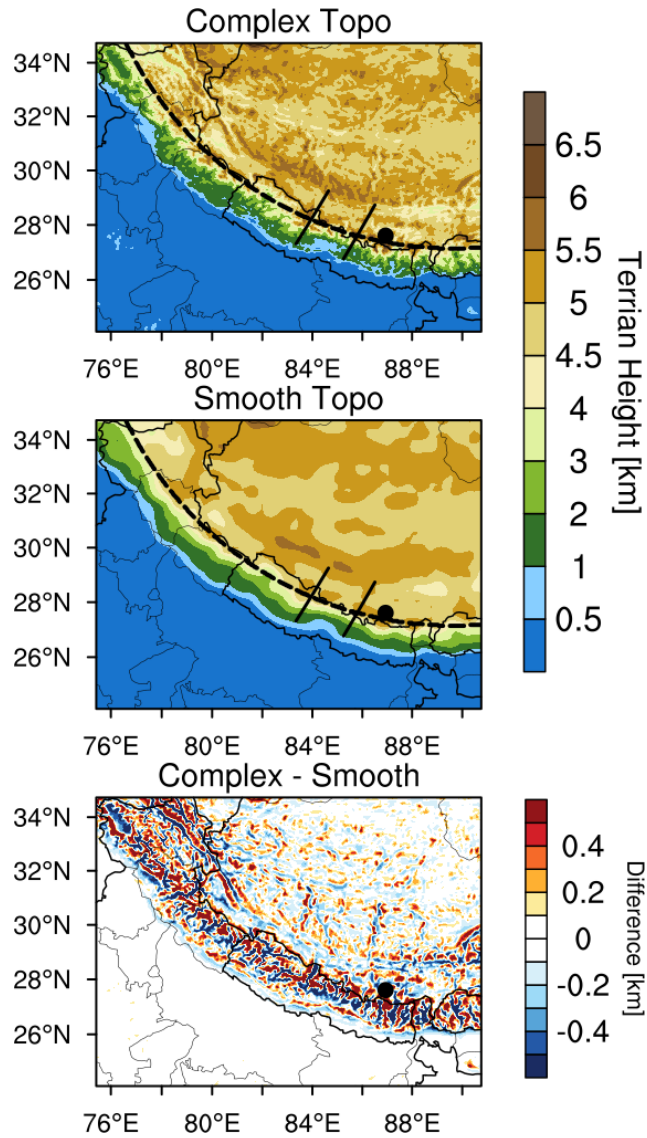
1278  
1279  
1280  
1281  
1282  
1283  
1284  
1285  
1286  
1287  
1288



1289  
1290  
1291  
1292  
1293  
1294  
1295  
1296  
1297  
1298  
1299  
1300  
1301  
1302  
1303  
1304  
1305  
1306  
1307  
1308

**Figure 2.** The thickness of each vertical layer in the simulations (54 layers in total).

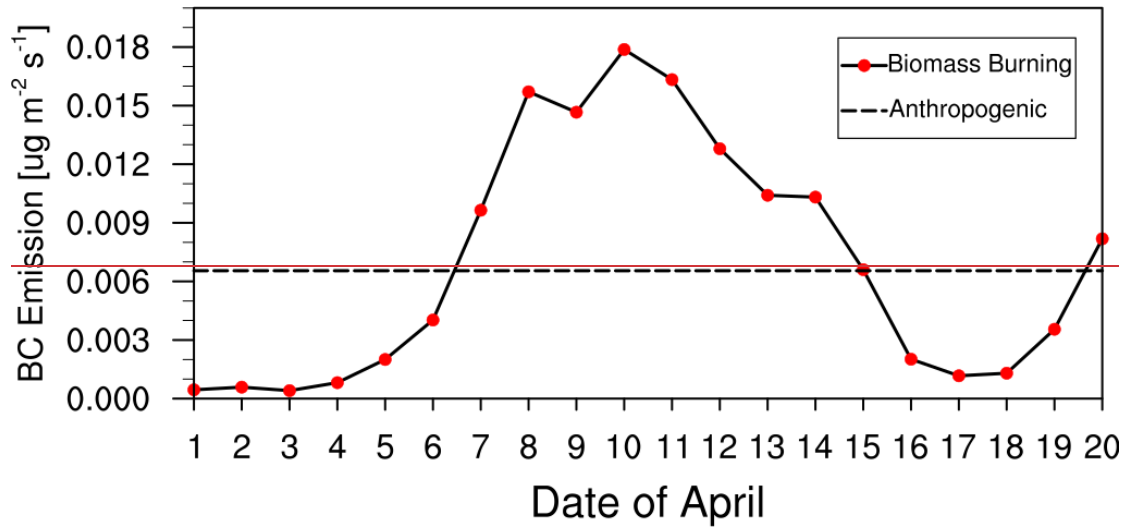
1309  
1310  
1311  
1312  
1313  
1314  
1315  
1316  
1317  
1318  
1319



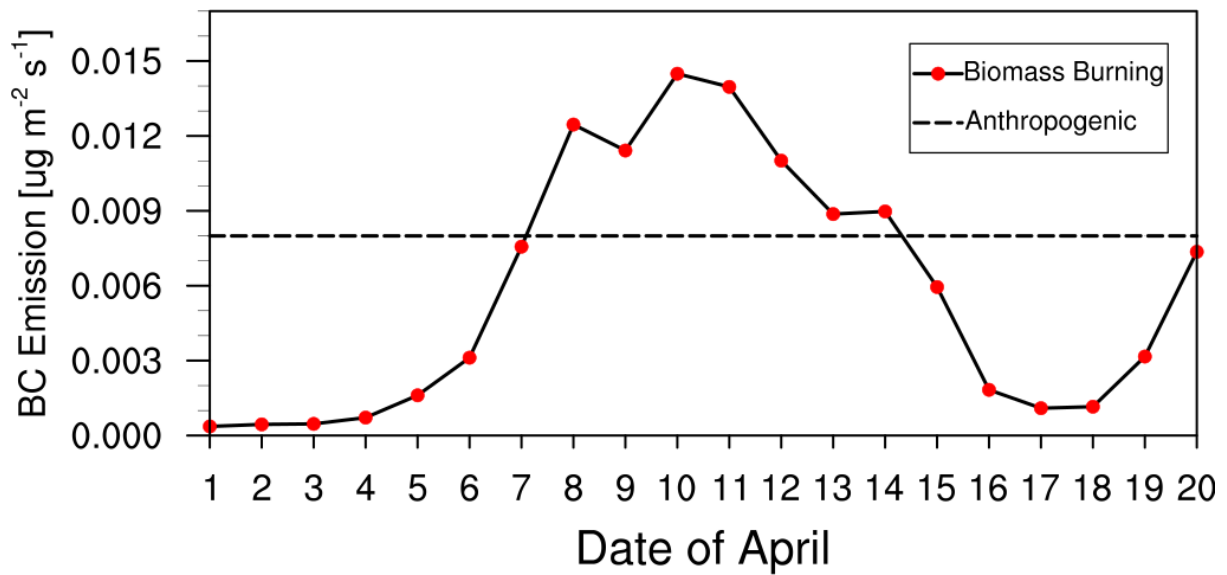
1320  
1321  
1322  
1323  
1324  
1325  
1326  
1327  
1328

**Figure 3.** Spatial distributions of terrain height from the dataset at 20-4-km (Smooth Topo) and 4 km-resolution (Complex Topo) and bilinearly interpolated from the 20-km resolution dataset (Smooth Topo). The one dash line and two solid lines represent the cross sections for analysis in the following.

1329  
1330  
1331  
1332  
1333  
1334  
1335  
1336  
1337  
1338  
1339



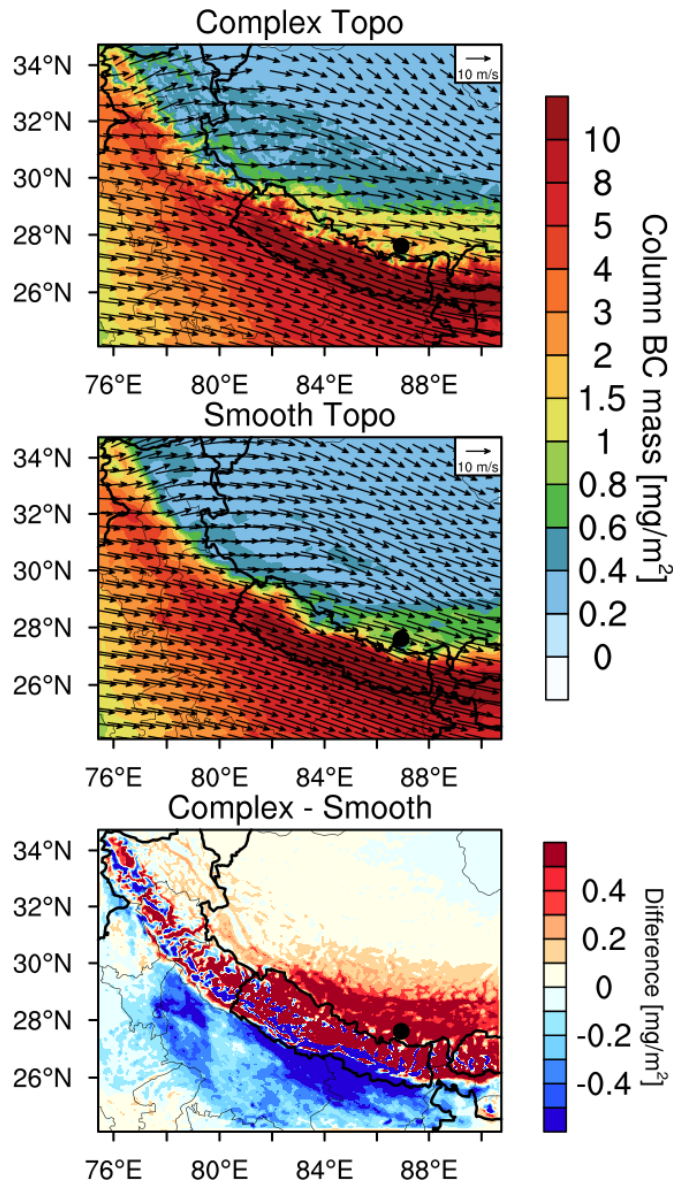
1340  
1341  
1342



1343  
1344  
1345  
1346  
1347  
1348  
1349  
1350

**Figure 4.** Time series of area-averaged daily fire emissions between 26°N and 29°N over the simulation domain at 4-km resolution (The dash line in the figure represents the anthropogenic emissions).

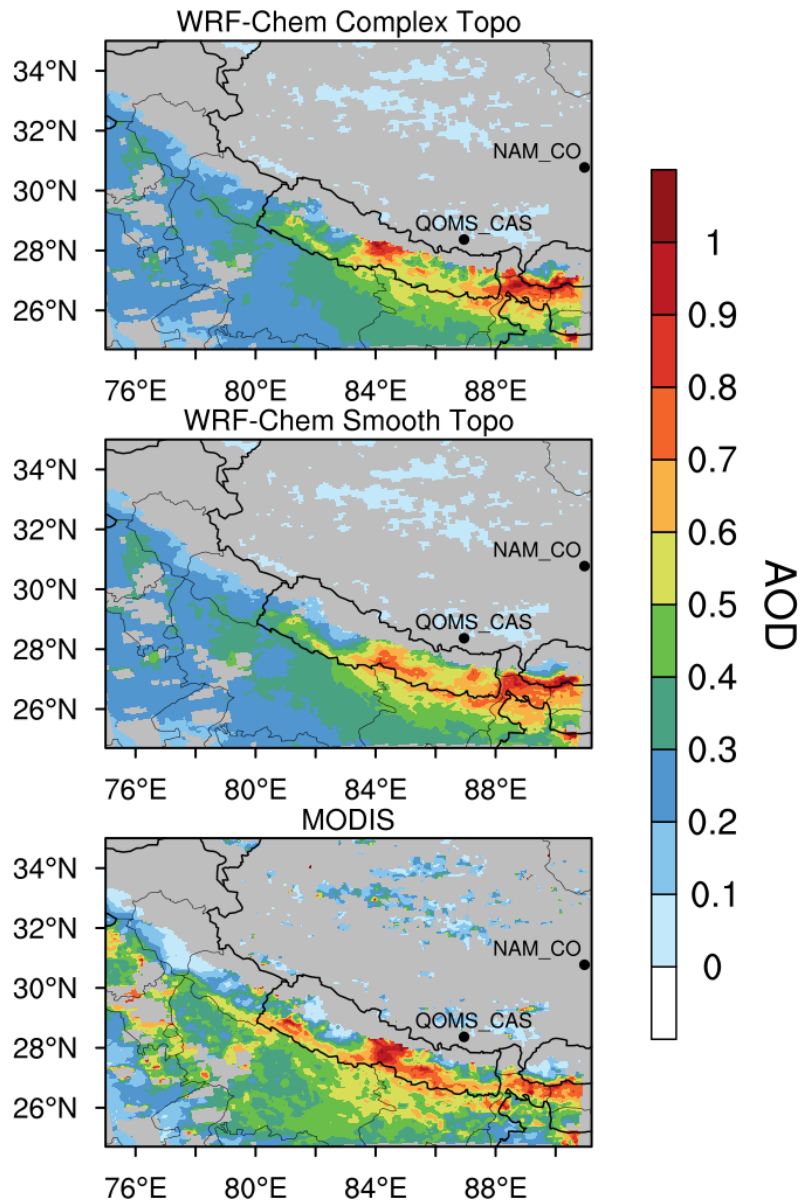
1351  
1352  
1353  
1354  
1355  
1356  
1357  
1358  
1359  
1360  
1361  
1362  
1363  
1364  
1365  
1366  
1367  
1368  
1369  
1370  
1371  
1372  
1373  
1374



1375  
 1376 **Figure 5.** Spatial distributions of column integrated BC mass and the horizontal wind field at  
 1377 500 hPa from the simulations with complex and smooth topography (Complex Topo and  
 1378 Smooth Topo) averaged for April 1-20, 2016. The difference between the two is also shown.  
 1379

1380  
 1381  
 1382  
 1383  
 1384  
 1385  
 1386  
 1387  
 1388  
 1389  
 1390  
 1391  
 1392  
 1393

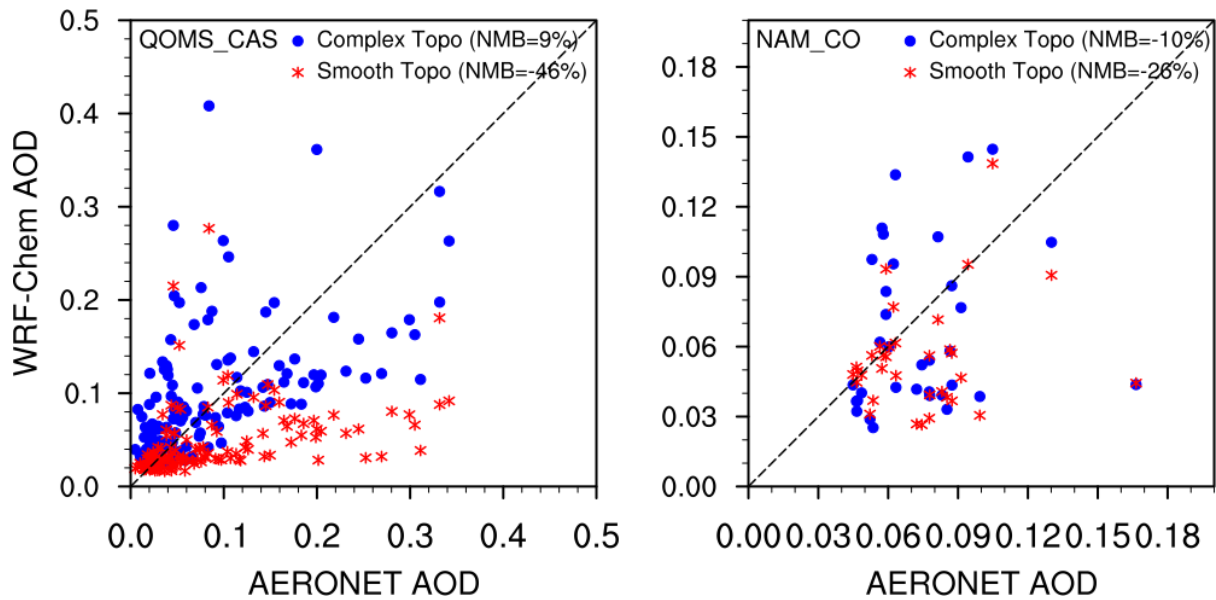
1394  
1395



1396  
1397  
1398  
1399  
1400  
1401  
1402  
1403  
1404  
1405  
1406  
1407  
1408  
1409  
1410  
1411  
1412

**Figure 6.** Spatial distributions of AOD from the MODIS retrievals and the simulations with complex and smooth topography averaged for April 1-20, 2016. The two black dots represent the two AERONET sites over the TP (QOMS\_CAS, 86.95°E, 28.36°N; NAM\_CO, 90.96°E, 30.77°N).

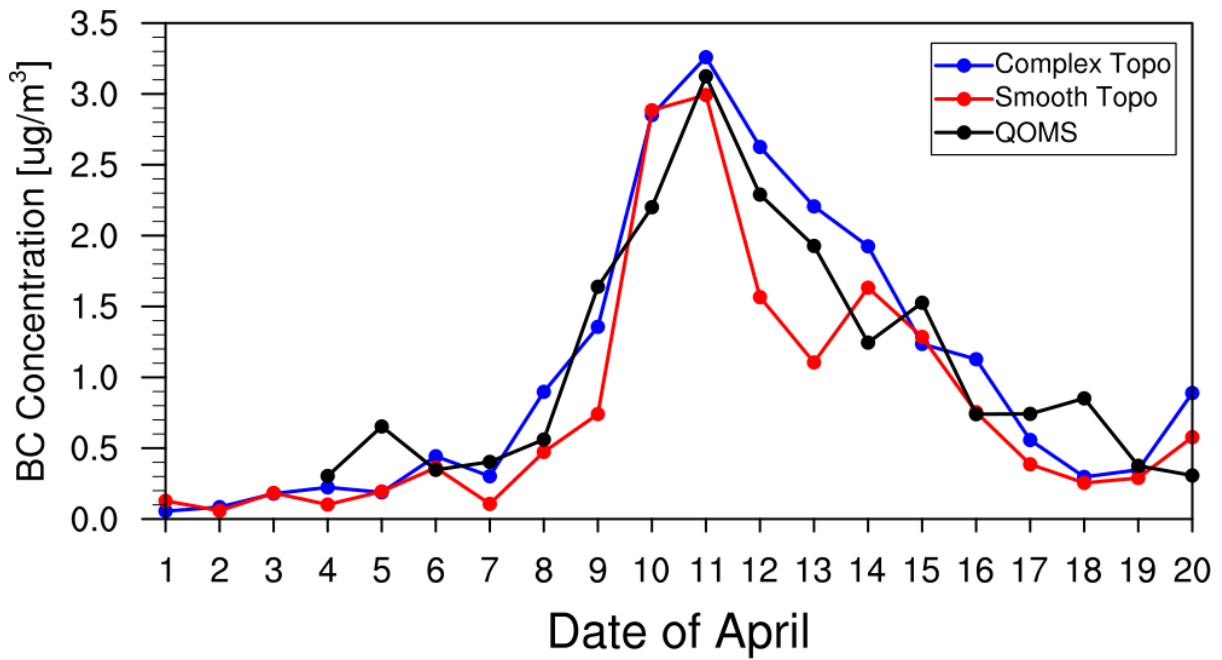
1413  
1414  
1415



1416  
1417  
1418  
1419  
1420  
1421  
1422  
1423  
1424  
1425  
1426  
1427  
1428  
1429  
1430  
1431  
1432  
1433  
1434  
1435  
1436  
1437  
1438  
1439  
1440  
1441  
1442  
1443  
1444  
1445  
1446

**Figure 7.** Hourly AOD from the measurements of AERONET and simulations by WRF-Chem at the two sites over the TP (QOMS\_CAS, 86.95°E, 28.36°N; NAM\_CO, 90.96°E, 30.77°N) for April 1-20, 2016.

1447  
1448

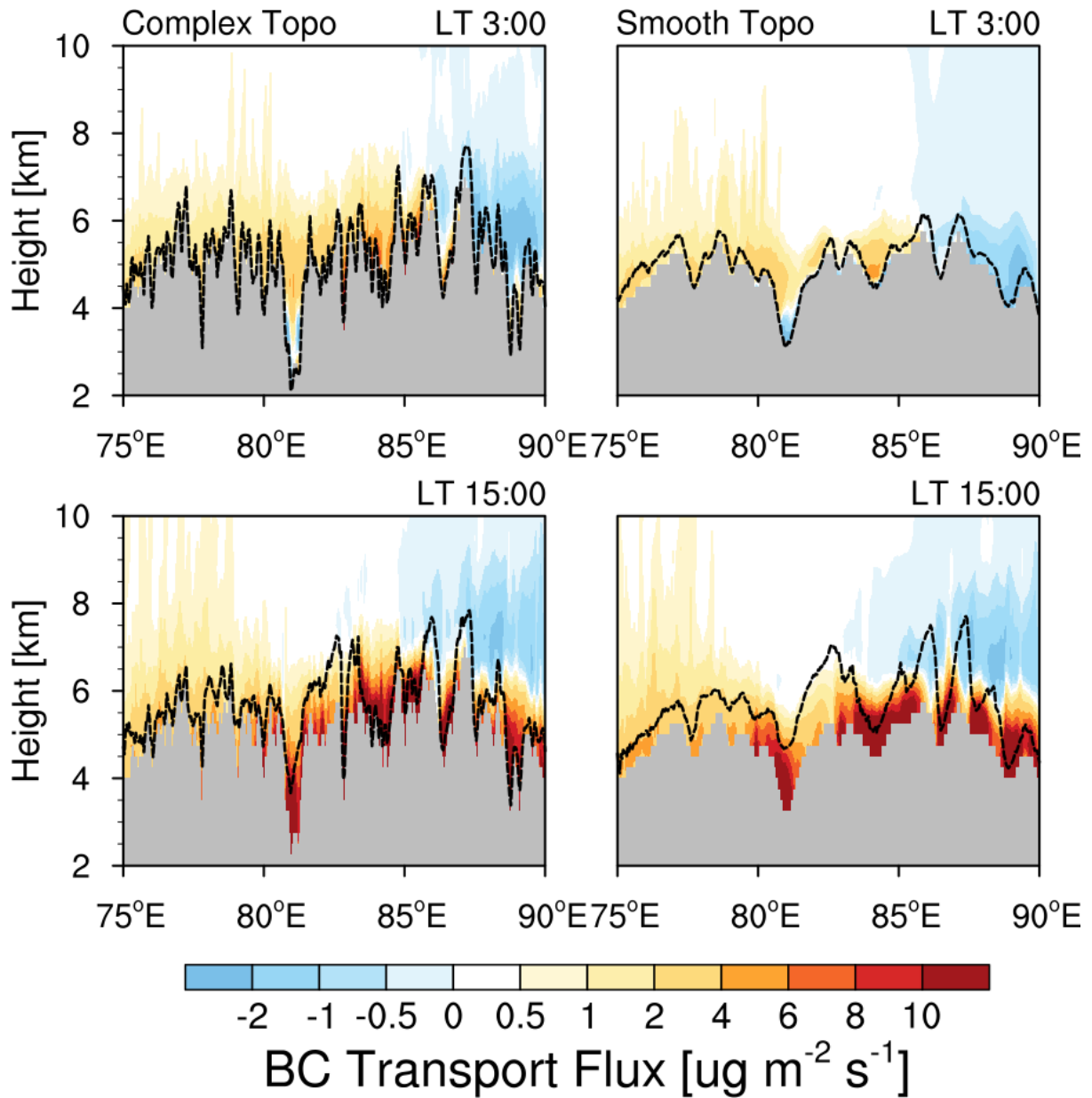


1449  
1450  
1451  
1452  
1453  
1454  
1455  
1456  
1457  
1458  
1459  
1460  
1461  
1462  
1463  
1464  
1465  
1466  
1467  
1468  
1469  
1470  
1471  
1472  
1473  
1474  
1475  
1476  
1477  
1478  
1479

**Figure 8.** The simulated (colored) and observed (black) temporal variability of near-surface BC mass concentration at the measurement station during April 1-20 in 2016.



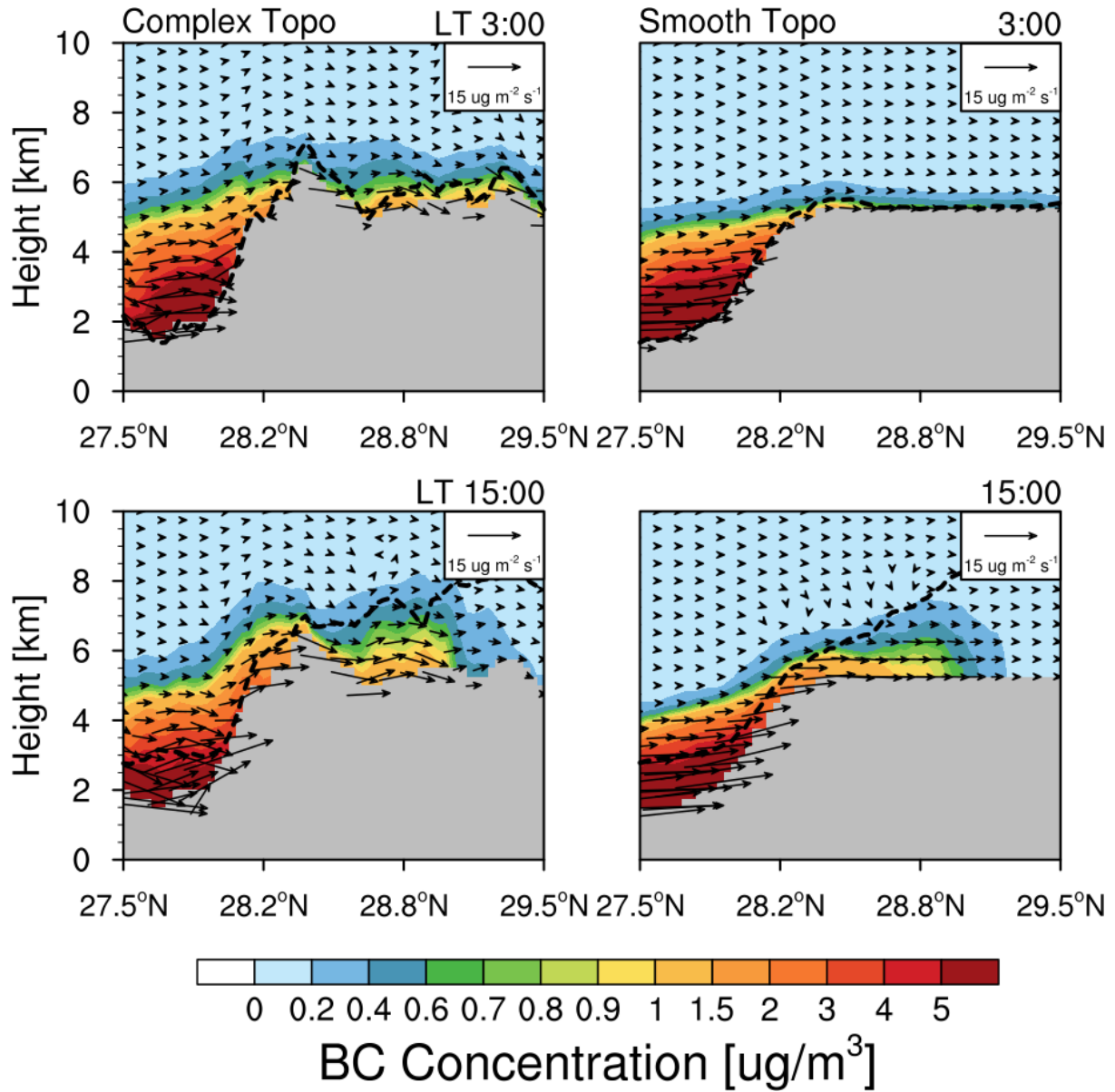
1480  
1481



1482  
1483  
1484  
1485  
1486  
1487  
1488  
1489  
1490  
1491  
1492  
1493  
1494  
1495  
1496  
1497

**Figure 9.** Longitude-height cross section of BC transport flux along the cross line (shown as the black dash line in Fig. 3) from the simulations with complex and smooth topography at local time (LT) 03:00 and 15:00 averaged for April 1-20. The PBL height along the cross section is shown here as the black dash line.

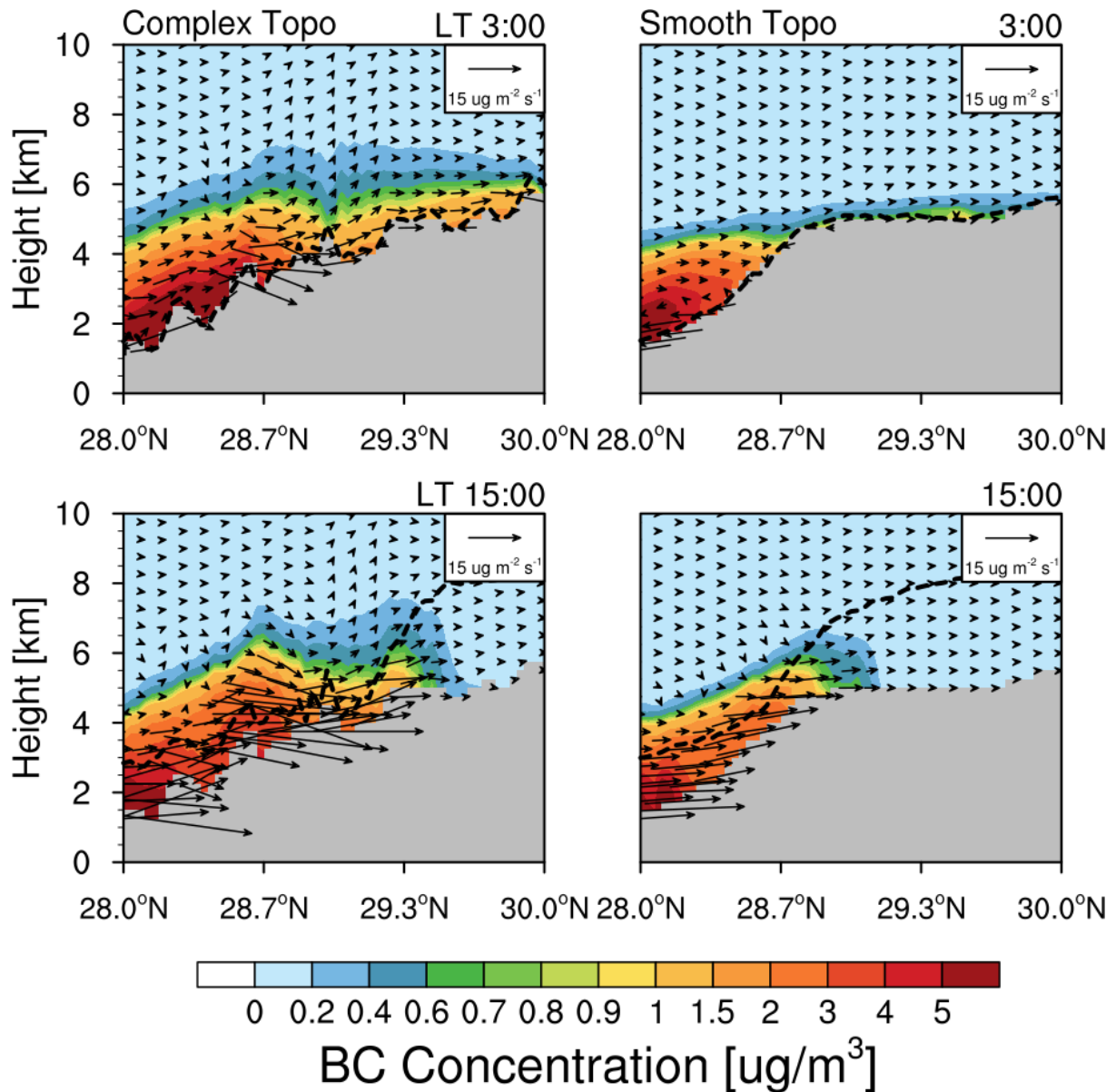
1498  
1499  
1500  
1501



1502  
1503  
1504  
1505  
1506  
1507  
1508  
1509  
1510  
1511  
1512  
1513  
1514  
1515  
1516

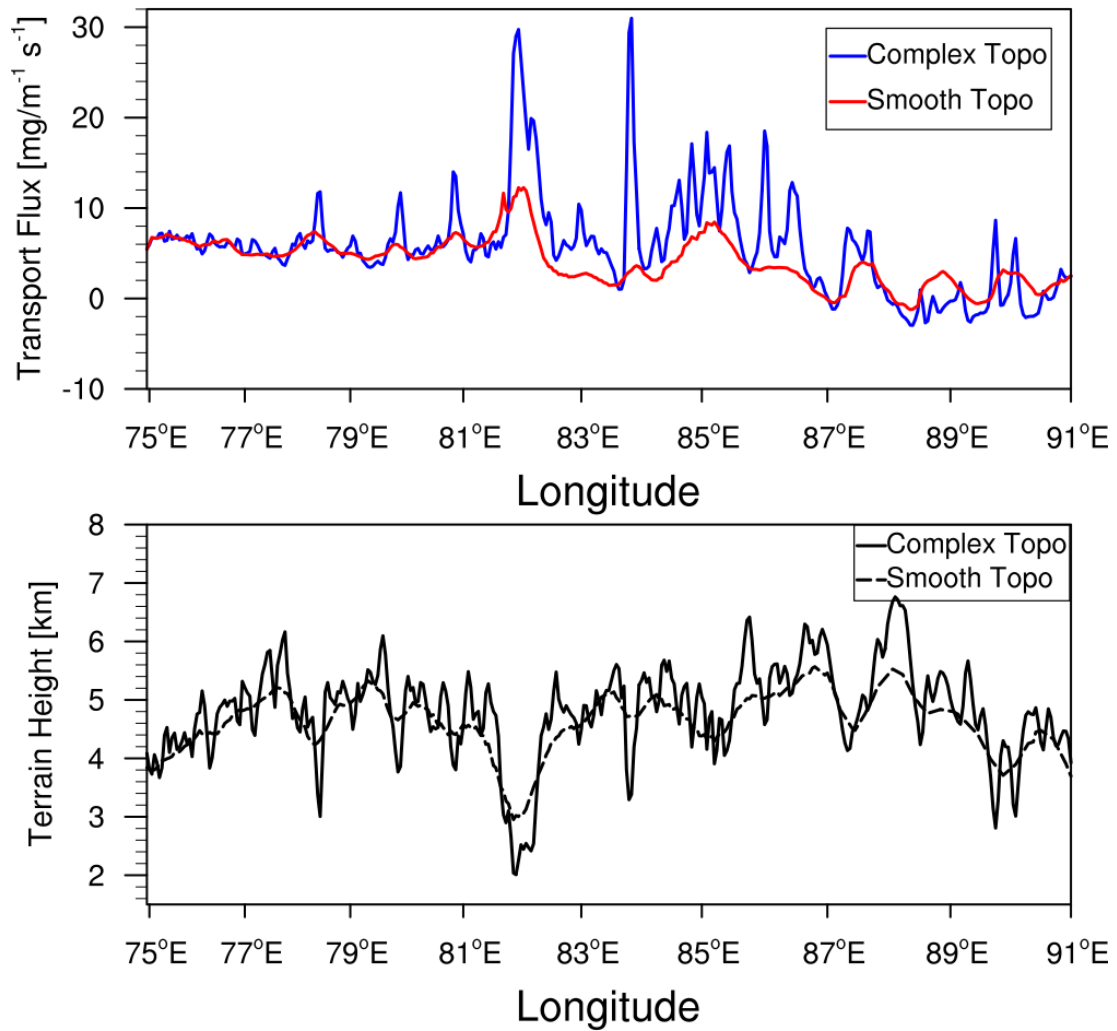
**Figure 10.** Latitude-height cross section of BC flux (vector) across the mountain (shown as the East black solid line in Fig.3) from the simulations with complex and smooth topography at local time (LT) 03:00 and 15:00 averaged for April 1-20, 2016. Contour represents the BC concentration.

1517  
1518



1519  
1520  
1521  
1522  
1523  
1524  
1525  
1526  
1527  
1528  
1529  
1530  
1531  
1532  
1533  
1534

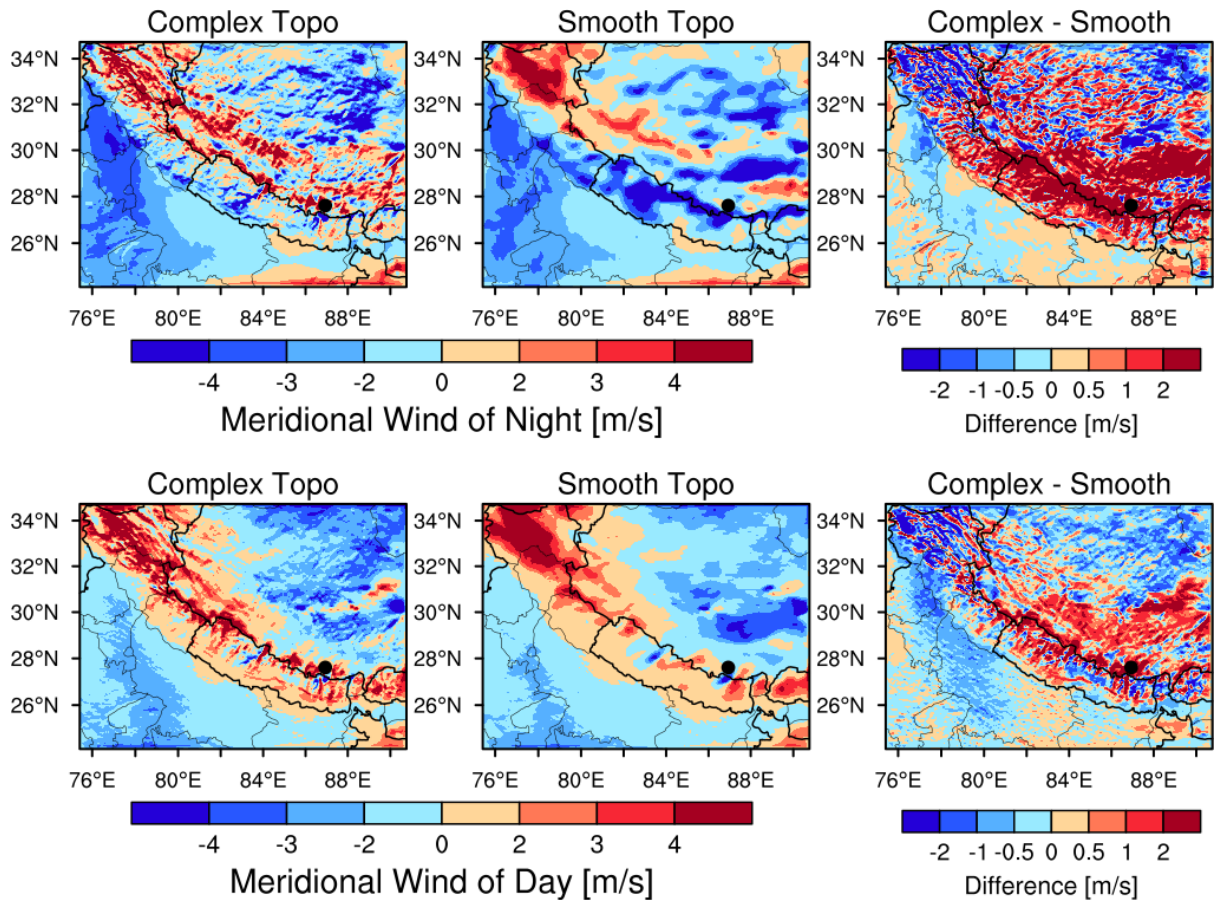
**Figure 11.** Latitude-height cross section of BC flux (vector) along the valley (shown as the West black solid line in Fig. 3) from the simulations with complex and smooth topography at local time (LT) 03:00 and 15:00 averaged for April 1-20, 2016. Contour represents the BC concentration.



1535  
 1536  
 1537  
 1538  
 1539  
 1540  
 1541  
 1542  
 1543  
 1544  
 1545  
 1546  
 1547  
 1548  
 1549  
 1550  
 1551  
 1552  
 1553  
 1554  
 1555  
 1556  
 1557

**Figure 12.** Longitudinal distribution of integrated BC mass flux along the cross section in Fig. 3 from the simulations with complex and smooth topography. The black lines represent the terrain heights with different topography.

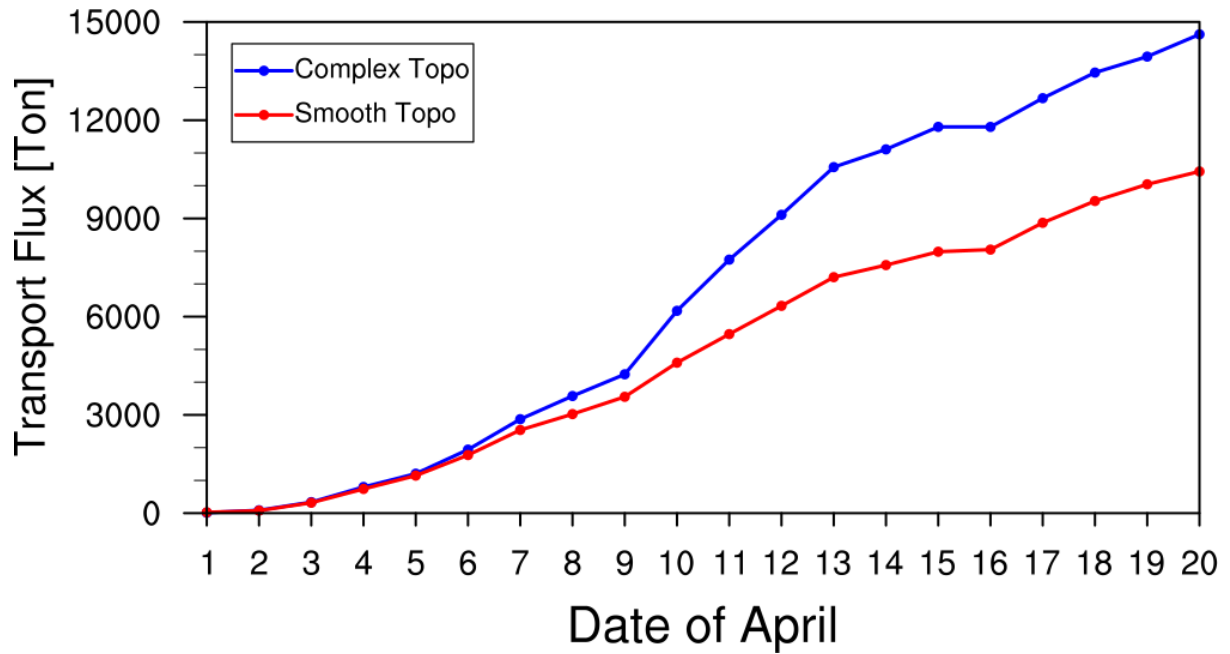
1558  
1559  
1560



1561  
1562  
1563  
1564  
1565  
1566  
1567  
1568  
1569  
1570  
1571  
1572  
1573  
1574  
1575  
1576  
1577  
1578  
1579  
1580  
1581  
1582  
1583  
1584

**Figure 13.** Spatial distributions of meridional wind speed averaged within 500 m above the ground for day and night during April 1-20, 2016 from the simulations with complex and smooth topography. The difference between the two is also shown. Nighttime is defined as local time 21:00-6:00, and daytime is defined as 9:00-18:00. Positive value denotes southerly, and negative value denotes northerly.

1585



1586

1587

**Figure 14.** Accumulated integrated total transport flux of BC across the Himalayas estimated from the simulations with complex and smooth topography during April 1-20, 2016.

1588

1589

1590

1591

1592

1593

1594

1595

1596

1597

1598

1599

1600

1601

1602

1603

1604

1605

1606

1607

1608

1609

1610

1611

1612

1613

1614

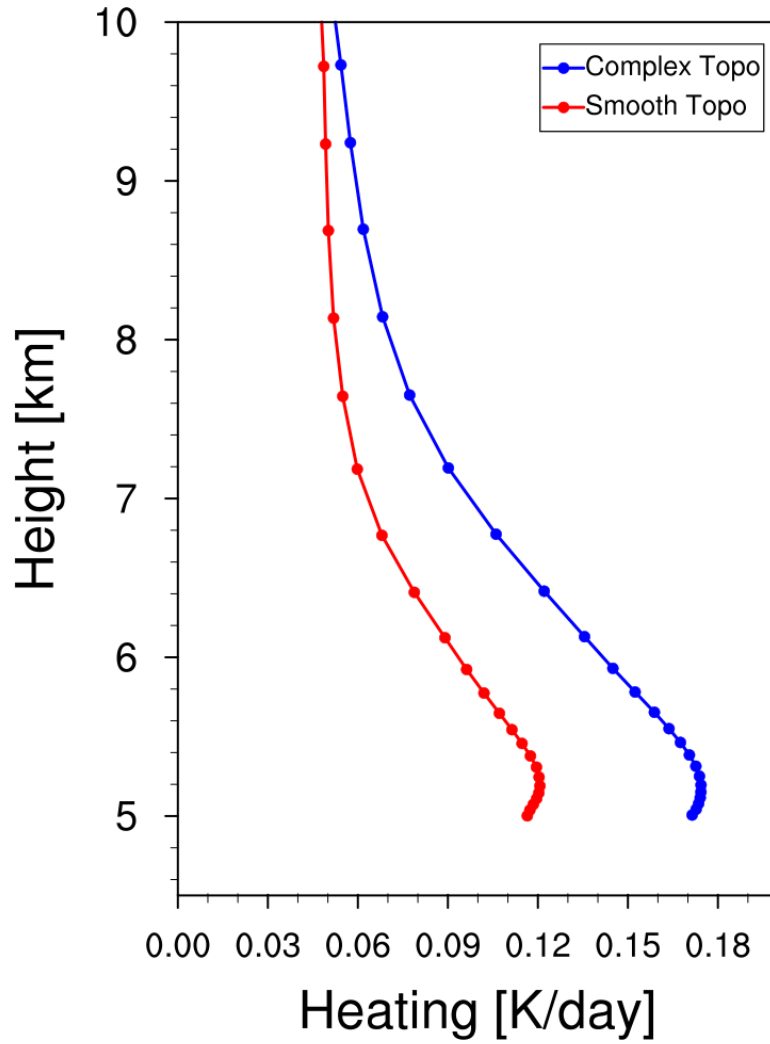
1615

1616

1617

1618

1619

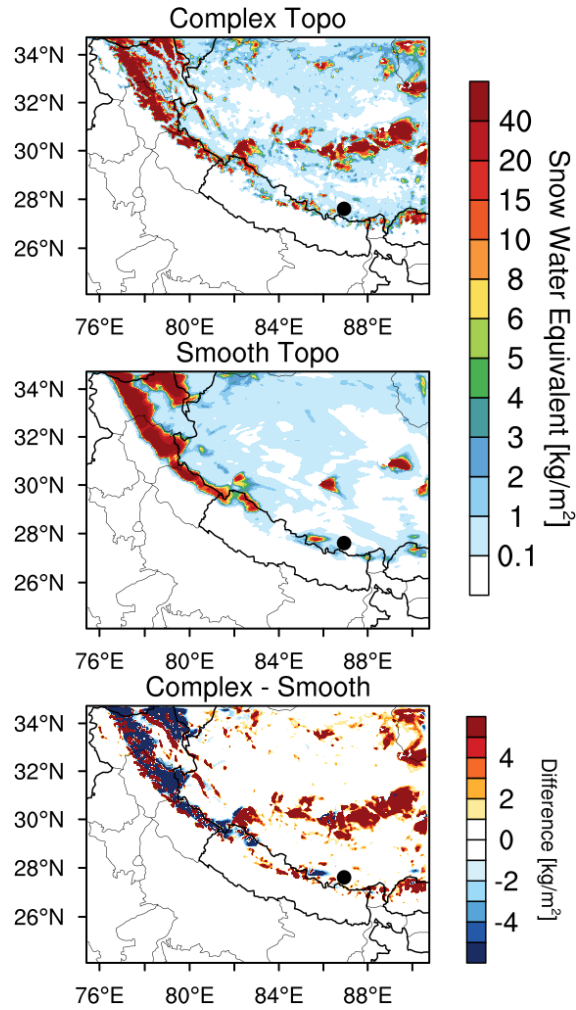


1620  
1621  
1622  
1623  
1624  
1625  
1626  
1627  
1628  
1629  
1630  
1631  
1632  
1633  
1634  
1635  
1636  
1637  
1638  
1639  
1640  
1641

**Figure 15.** Vertical profiles of BC induced radiative heating rate in the atmosphere averaged over the TP (with elevation > 4 km) from the simulations with complex and smooth topography during April 1-20, 2016.



1642

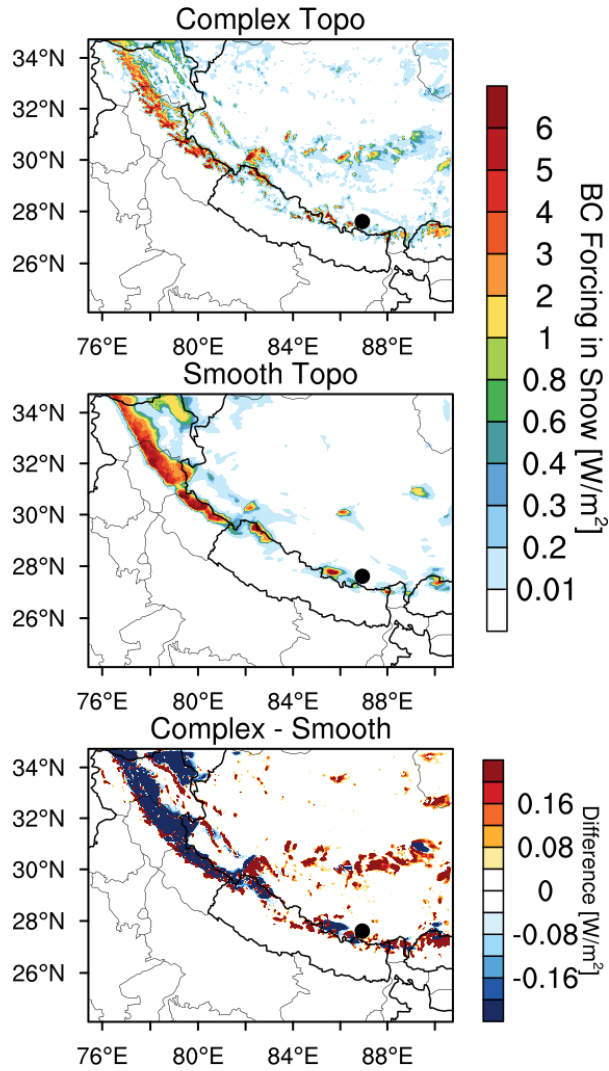


1643  
1644  
1645  
1646  
1647  
1648  
1649  
1650  
1651  
1652  
1653  
1654  
1655  
1656  
1657  
1658  
1659  
1660  
1661  
1662  
1663  
1664  
1665

**Figure 16.** Spatial distributions of snow water equivalent averaged for April 1-20, 2016 from the simulations with complex and smooth topography. The difference between the two is also shown.



1666



1667  
1668  
1669  
1670  
1671  
1672  
1673  
1674  
1675  
1676  
1677  
1678

**Figure 17.** Spatial distributions of BC radiative forcing in the surface snow averaged for April 1-20, 2016 from the simulations with complex and smooth topography. The difference between the two is also shown.